Breathing dynamics of the few-body Bose polaron in a species-selective harmonic trap

Maxim Pyzh[1,*] and Peter Schmelcher[1,2,†]

[1]*Zentrum für Optische Quantentechnologien, Universität Hamburg, Luruper Chaussee 149, 22761 Hamburg, Germany*

[2]*The Hamburg Centre for Ultrafast Imaging, Universität Hamburg, Luruper Chaussee 149, 22761 Hamburg, Germany*

(Received 20 July 2021; accepted 22 March 2022; published 8 April 2022)

We perform an extensive numerical study on the breathing dynamics of a few-body Bose polaron setup in a one-dimensional species-selective harmonic trap. The dynamics is triggered by a quench of the impurity trap. The excitation of the background majority atoms is mediated via the majority-impurity interaction. The breathing spectrum is obtained for different numbers of majority particles, several values of the majority-component interaction strengths, and trap ratios. It is further compared to the breathing spectrum of a particle-balanced few-body Bose-Bose mixture. In particular, for equal postquench traps the employed protocol allows to couple states of different center-of-mass parity in contrast to species-symmetric trap quenches. Among the participating eigenstates we identify one having odd center-of-mass parity and even global parity. The breathing frequency induced by this state is a monotonically decreasing function of the coupling parameter. Importantly, in order to be numerically observable, it requires the entanglement between the species to be taken into account. We demonstrate this by comparing the numerically exact results obtained by means of the multilayer multiconfiguration time-dependent Hartree method for mixtures to the ones of a species mean-field ansatz. The entanglement-sensitive breathing frequency persists also for unequal postquench traps where the center of mass cannot be decoupled. Finally, we analyze the impact of global parity symmetry on the breathing dynamics by initializing a state of odd global parity. We evidence a striking resemblance to the breathing spectrum of the ground state, but find also some additional modes.

DOI: 10.1103/PhysRevA.105.043304

I. INTRODUCTION

The polaron concept was introduced quite some time ago by Landau and Pekar [1,2] to describe the motion of an electron in a crystalline material. The notion of an emerging quasiparticle dressed by low-energy excitations of the underlying medium has vastly expanded since its foundation finding broad applications in different areas of physics such as organic semiconductors, polymers, nanowires, quantum dots, and high-temperature superconductors [3–5]. Since the advent of ultracold gases [6,7], a promising experimental platform has emerged allowing to investigate fundamental many-body quantum processes [8] with an exquisite tunability of the underlying interactions and trapping geometries. In particular, the ability to combine different species [9] and the precise control over the number of particles [10] made it possible to experimentally prepare an impurity in a many-body environment of bosons [11–16] or fermions [17–21], leading to what is nowadays termed Bose [22] and Fermi polaron [23,24], respectively. A mapping to the Fröhlich Hamiltonian [25] for the polaron problem can be established while all the Hamiltonian parameters can be addressed individually. The tunability of interactions via Feshbach resonances [26,27] provides access to highly correlated and entangled regimes challenging the theorists to go beyond the weak coupling Fröhlich paradigm [28–34].

The correlations are in particular enhanced in quasi-one-dimensional (1D) systems [35]. A comparatively tight transverse confinement freezes the perpendicular motion of particles and additionally affects the effective 1D interactions known as confinement-induced resonances [36–38]. A prominent example of a strongly correlated 1D system is the Tonks-Girardeau gas [39–41]. In contrast to higher dimensions, where a lower particle density implies weaker correlations, in 1D lower densities lead to stronger interactions. It makes the study of low-density few-body systems of particular interest triggering significant research efforts [42]. At the same time, this represents a great challenge requiring sophisticated numerical techniques able to account for all the relevant correlations [43] when characterizing the static properties or the many-body dynamics, such as the density matrix renormalization group (DMRG) [44] or the multilayer multiconfiguration time-dependent Hartree method for bosons and fermions (ML-MCTDHX) [45]. In species-selective trapping geometries [12,46,47] the inhomogeneity of the medium and the localization length of the impurity impact significantly the degree of correlations [48–50] opening interesting perspectives but requiring also new approaches since the translation symmetry is broken making the well-established technique, the Lee-Low-Pines transformation [51], inapplicable.

In this work, we investigate the low-energy excitations of a few-body Bose polaron trapped harmonically in one spatial dimension. Elementary excitations [52,53] are of fundamental importance to understand the dynamical response of a physical system subject to a weak perturbation in terms of excited eigenstates and respective eigenenergies. Here, we focus on

*mpyzh@physnet.uni-hamburg.de
†pschmelc@physnet.uni-hamburg.de

the so-called quantum breathing modes. They are characterized by an oscillatory compression and expansion of the one-body density reminiscent of a respiratory movement. On account of their strong sensitivity to the system's parameters such as interactions, trap geometry, and spin statistics, they have been established as a reliable diagnostic tool to access the ground-state properties of a system [54], for precision measurements of the scattering lengths [55] and even as a sensitive test of the equation of state at unitarity [56].

A number of experiments have observed the breathing motion of harmonically or lattice trapped Bose-Einstein condensates (BEC) [55,57–62] and mixtures of bosons and/or fermions [12,17,63–65]. The single-component breathing is theoretically well understood in the many-body case for contact [66–69], power-law [70–72], and dipolar [73] interactions. In a 1D harmonic trap of frequency ω at zero temperature, one has identified two breathing modes: (i) center-of-mass breathing of constant frequency $\Omega_{\text{c.m.}} = 2\omega$ and (ii) interaction-sensitive relative motion mode starting at $\Omega_{rel} = 2\omega$ for an ideal gas (BEC regime), dropping to $\Omega_{rel} = \sqrt{3}\omega$ at weak repulsive interactions (mean-field Thomas-Fermi regime) and finally saturating back to $\Omega_{rel} = 2\omega$ in the limit of strong interactions (Tonks-Girardeau regime). The frequency values at intermediate interactions are well approximated via a sum-rule approach [66,67,74–76] and the overall frequency curve features a single minimum between the BEC and TG limits. The curvature in-between those limits and the exact minimum location are quite sensitive to the number of particles and beyond-mean-field effects are often indispensable for a correct quantitative description [77–82].

The breathing dynamics turns out to be even richer for a multicomponent mixture of bosons [83–89], fermions [17,76], and combination of the two [90–93]. Theoretically, up to four breathing frequencies can be extracted from the density width oscillations of both components depending on the interplay between interactions and particle-number imbalance: breathing of the center of mass, the relative motion for each component, and the relative intercomponent motion owing to the particles' distinguishability. The frequencies of the three relative modes behave in a similar fashion as the frequency of the relative mode encountered in the single-component case. To the best of our knowledge, both components have been considered to be equally trapped, allowing for a separation of the center-of-mass motion. In our work, we make use of species-selective trapping potentials to find out (i) how initially different traps would affect the breathing behavior in combination with (ii) how compressing the trap of only one component, the impurity, would impact the breathing motion of the second component, the majority, depending on the intercomponent coupling. For different system parameters, we classify the breathing modes according to their relative amplitude in the Fourier power spectrum obtained by applying a compressed sensing (CS) [94] algorithm to breathing observables evaluated via ML-MCTDHX. Furthermore, we study the role of intercomponent entanglement and parity symmetries on the breathing response. We identify an entanglement-sensitive mode whose frequency is a monotonically decreasing function of the majority-impurity interaction.

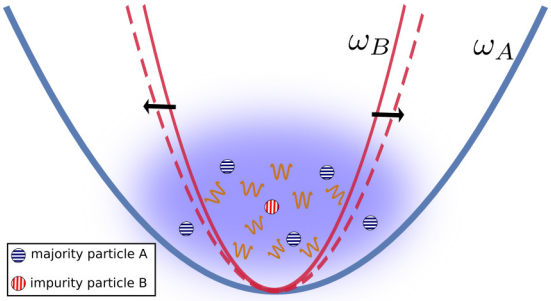

FIG. 1. The impurity (species B indicated by a red circle with a vertically dashed filling) in a harmonic trap of frequency ω_B (red thin solid line) is immersed in a cloud of majority atoms (species A indicated by a blue blurred ellipse) subject to a different parabolic confinement of frequency ω_A (blue broad solid line). The breathing dynamics is initiated by quenching the trap of the impurity (red dashed line) inducing thereby excitations (orange waves) in the composite system via the majority-impurity interaction.

This work is structured as follows. In Sec. II we introduce our setup and Hamiltonian. The numerical approach is discussed in Sec. III A. We use ML-MCTDHX for state initialization, subsequent dynamics, and evaluation of breathing observables. The oscillation frequencies are extracted by means of a CS algorithm outlined in Sec. III B. The results presented in Sec. IV are categorized in four subtopics: an overview of breathing modes in a particle-balanced few-body Bose-Bose mixture [88] (Sec. IV A) for later reference, the breathing spectra in the current Bose polaron setup for different majority-component interactions and particle-number ratio (Sec. IV B), the impact of impurity localization length (Sec. IV C), and, finally, the role of global parity symmetry for the breathing response (Sec. IV D). In Sec. V we provide a summary and draw conclusions in Sec. VI.

II. SETUP AND HAMILTONIAN

We consider a few-body mixture of two bosonic components (see Fig. 1). A component $\sigma \in \{A, B\}$ contains N_σ particles of mass m_σ, which experience a quasi-one-dimensional parabolic confinement with trap frequency ω_σ and interact internally via contact pseudointeraction of strength g_σ. The components are coupled via an interspecies contact interaction of strength g_{AB}. We assume equal masses and introduce harmonic units of component A as our natural units, i.e., $l_A = \sqrt{\hbar/m\omega_A}$ for length, $\hbar\omega_A$ for energy and $1/\omega_A$ for time. The corresponding Hamiltonian reads as follows:

$$\begin{aligned} H &= H_A + H_B + H_{AB} \\ &= \sum_{i=1}^{N_A}\left(-\frac{1}{2}\frac{\partial^2}{\partial x_i^2} + \frac{1}{2}x_i^2\right) + g_A\sum_{i<j}^{N_A}\delta(x_i - x_j) \\ &\quad + \sum_{i=1}^{N_B}\left(-\frac{1}{2}\frac{\partial^2}{\partial y_i^2} + \frac{1}{2}\eta^2 y_i^2\right) + g_B\sum_{i<j}^{N_B}\delta(y_i - y_j) \\ &\quad + g_{AB}\sum_{i=1}^{N_A}\sum_{j=1}^{N_B}\delta(x_i - y_j), \end{aligned} \tag{1}$$

where x_i (y_i) denotes the position of the ith particle in the A (B) component.

The A component is referred to as the majority species. It has $N_A \in \{5, 10\}$ particles. The B component consists of a single particle, $N_B = 1$, and we call it the impurity. The majority component is either noninteracting ($g_A = 0$) or features a weakly attractive or repulsive interaction ($g_A = \pm 0.5$). The majority-impurity coupling covers values from weakly attractive to intermediate repulsive $g_{AB} \in [-0.5, 2.0]$. The trap ratio covers cases of equal traps ($\eta = 1$), a "broad" impurity ($\eta = 0.51$) and a "narrow" impurity ($\eta = 4$). The weak-to-intermediate interaction regimes considered here cover most of ground-state density configurations encountered in bosonic mixtures including miscible phase, core-shell separation [49,88,95,96], and composite fermionization [97,98]. The strongly correlated regimes such as full fermionization or the spin-chain configurations [99,100] are computationally challenging and require a fundamentally different treatment than the one employed in this work.

The Hamiltonian (1) possesses a *global reflection symmetry*, corresponding to a map $x_i \mapsto -x_i$ and $y_j \mapsto -y_j$ for all i, j. It implies that the energy eigenstates can be chosen to have a definite global parity, i.e., to be eigenstates of the above operation with eigenvalues $+1$ (even) or -1 (odd). An eigenstate can be thus classified as being of even or odd global parity. We prepare our system either in the ground state (even global parity in Secs. IV B and IV C) or in the first excited state (odd global parity in Sec. IV D) at $\eta_0 = 1.05\eta$ of Eq. (1), the *prequench* Hamiltonian. To initiate the breathing dynamics we slightly relax the trap of the impurity from η_0 to η and propagate the state with this *postquench* Hamiltonian. The majority species is set in breathing motion indirectly via the coupling to the impurity. Importantly, the two global parity subspaces are not coupled by the trap quench. Thus, an initial state of definite global parity will remain in the corresponding subspace. We can thus investigate the role of global parity on the breathing response.

The breathing motion can be monitored in the one-body densities $\rho_1^\sigma(z, t)$ as their widths expand and contract periodically in time. Alternatively, one can analyze the time evolution of the corresponding breathing observables $\langle \hat{O} \rangle_t$ with $\hat{O} = \sum_i \hat{x}_i^2$ for the majority species and $\hat{O} = \hat{y}^2$ for the impurity. The reason for equivalence is that the one-body density width, denoted as Δz, can be evaluated via $\langle \Delta z \rangle^2 = \langle z^2 \rangle - \langle z \rangle^2$. For an initial state of a definite global parity we have a reflection-symmetric one-body density which yields $\langle z \rangle = 0$. The oscillatory motion is usually composed of multiple contributions with amplitudes d_n and distinct frequencies Ω_n, i.e., $\langle \hat{O} \rangle_t = \sum_n d_n e^{-i\Omega_n t}$. Each of the oscillatory contributions in $\langle \hat{O} \rangle_t$ will be referred to as a *breathing mode* characterized by a distinct frequency. The origin of the breathing modes can be expressed in terms of system's eigenstates and related eigenenergies as follows. Upon a quench, several eigenstates $|\psi_n\rangle$ of the postquench Hamiltonian H with energy E_n become populated depending on the overlap c_n with the initial state $|\Psi(t_0)\rangle$, i.e., $c_n = \langle \psi_n | \Psi(t_0) \rangle$. The time signal $\langle \hat{O} \rangle_t = \sum_{n,m} c_m^* c_n \langle \psi_m | \hat{O} | \psi_n \rangle e^{-i\Omega_{n,m} t}$ oscillates with frequencies $\Omega_{n,m} = E_n - E_m$ for populated eigenstates $c_n c_m \neq 0$ as long as the transition matrix elements $\langle \psi_n | \hat{O} | \psi_m \rangle = O_{nm}$ are nonzero. Given a weak perturbation, we expect the lowest-energy eigenstate of even (odd) global parity $|\psi_{\text{ref}}\rangle$ to have the largest overlap with the even (odd) global parity initial state $|\Psi(t_0)\rangle$, i.e., $|c_0|^2 \approx 1$. For that reason, the major part of frequencies contained in the breathing observable $\langle \hat{O} \rangle_t$ are energy gaps between any of the populated eigenstates and the reference eigenstate, i.e., $\Omega_n = E_n - E_{\text{ref}}$. Oscillations among any different combination of eigenstates are of minor amplitude, so we do not focus on them by setting a suitable amplitude threshold. For convenience, when we refer to an eigenstate of a breathing mode we mean the eigenstate responsible for this mode while the reference state $|E_{\text{ref}}\rangle$ is usually clear within the context, unless we state otherwise. In case of "degenerate" energy gaps, i.e., equal energy gaps stemming from different eigenstate pairs, we do not differentiate which pairs actually contribute.

Finally, we would like to emphasize some fine subtleties between the species-asymmetric trap quench protocol employed in this work and the center-of-mass (c.m.) degree of freedom. First, for $\eta \neq 1$ the c.m. coordinate cannot be decoupled by any linear transformation. This is an important difference to species-symmetric traps at $\eta = 1$ where the c.m. coordinate provides an exact quantum number of the "free" c.m. harmonic oscillator. This becomes evident after employing a linear transformation to a set of Jacobi coordinates adapted to the Bose polaron problem, namely, relative coordinates of the majority species $r_j = \frac{1}{j} \sum_i^j x_i - x_{j+1}$ for $j \in \{1, \ldots, N_A - 1\}$, the global center of mass $R_{\text{c.m.}} = \frac{1}{(N_A+1)} (\sum_i^{N_A} x_i + y)$, and the relative coordinate characterizing the distance between the impurity and center of mass of the majority $R_{AB} = (\frac{1}{N_A} \sum_i^{N_A} x_i) - y$. Using this representation, the $R_{\text{c.m.}}$ degree of freedom decouples from the relative coordinates r_j and R_{AB} such that $H = H_{\text{c.m.}} + H_{rel}$, where $H_{\text{c.m.}}$ is a quantum harmonic oscillator of mass $N_A + 1$ and frequency $\omega = 1$, while H_{rel} is symmetric under the map $r_j \mapsto -r_j$ and $R_{AB} \mapsto -R_{AB}$. In this alternative relative-frame representation the Hamiltonian features a center-of-mass reflection symmetry, corresponding to a reflection operation $R_{\text{c.m.}} \mapsto -R_{\text{c.m.}}$. It implies that eigenstates can be chosen to have a definite c.m. parity, i.e., to be eigenstates of this operation with eigenvalues ± 1. We note that it is not equivalent to a global reflection symmetry since the latter applies additionally $r_j \mapsto -r_j$ and $R_{AB} \mapsto -R_{AB}$. In particular, an eigenstate may feature an even global parity, but be of odd c.m. parity and odd relative parity.

Second, we discuss several cases with the postquench Hamiltonian at $\eta = 1$, i.e., the corresponding eigenstates $|\psi_n\rangle$ have a definite c.m. harmonic oscillator quantum number. The initial state, on the other hand, is the ground state of the prequench Hamiltonian at $\eta_0 = 1.05$, i.e., it does not have such symmetry. Within the linear response regime, it can be shown that the occupation c_n of the eigenstate $|\psi_n\rangle$ is proportional to transition element $\langle \psi_n | y^2 | \psi_0 \rangle$ induced by the impurity trap quench operator. In particular, as y^2 is composed of a coupling term $\propto R_{\text{c.m.}} R_{AB}$, it is allowed for the initial state to be in a superposition of postquench eigenstates with different c.m. parity.

III. COMPUTATIONAL APPROACH AND ANALYSIS

In this work we use the multilayer multiconfiguration time-dependent Hartree method for mixtures to initialize a system

in its ground state by means of relaxation, i.e., propagation in imaginary time, for the state evolution following a trap quench of the impurity and to evaluate the expectation values of breathing observables for each species as a function of time. We outline the major idea of the method in Sec. III A along with the wave-function ansatz for the system at hand. We then apply a compressed sensing algorithm to retain the frequencies from breathing observables. In view of the fact that CS relies on the sparsity condition in the Fourier space, it is not used as a standard tool for frequency extraction from a time signal. In Sec. III B we discuss advantages of this method in the current application as compared to a straightforward Fourier transformation. In order to be self-contained, we also provide the implementation details.

A. ML-MCTDHX

To prepare the initial state $|\Psi(t_0)\rangle$ and to perform the subsequent time evolution $|\Psi(t)\rangle = e^{-iHt}|\Psi(t_0)\rangle$ with the time-independent Hamiltonian H from Eq. (1) we employ the *multilayer multiconfiguration time-dependent Hartree method for mixtures* of indistinguishable particles, for short, ML-X [45,101,102]. The core idea behind ML-X is to expand the many-body wave function in a properly symmetrized product state basis, the so-called Fock states, such that the underlying single-particle functions (SPFs) are *time dependent*. These are variationally optimized during the time evolution to provide a more "compact" description compared to Fock states composed of time-independent SPFs. Compact means that in general much less SPFs are required reducing thus the Fock space dimension while retaining a similar degree of accuracy.

As the system evolves, the many-body state travels through different subspaces of the complete Hilbert space. If the Fock basis is fixed, in general a large set of SPFs is required to cover all the relevant subspaces. Many configurations become "actively" populated during the time evolution, though not necessarily all of them at the same time with a fraction staying or becoming inactive. Even when all of Fock states are populated, we may rotate the basis by choosing a different set of SPFs until, eventually, we end up with a more compact representation. Given a truncated Fock space, ML-X rotates the basis vectors such as to find the best possible representation of the exact many-body state at each instant of time. In other words, it looks for the current "active" subspace. Once the truncated variationally evolving Fock space becomes large enough to contain the (major part of) "active" subspace, the representation of $|\Psi(t)\rangle$ given by ML-X is considered optimal.

The underlying wave-function ansatz for the Bose polaron problem belonging to Eq. (1) is expanded in two layers (multilayer):

$$|\Psi(t)\rangle = \sum_{i=1}^{S} \sqrt{\lambda_i(t)}\,\left|\Psi_i^A(t)\right\rangle \otimes \left|\Psi_i^B(t)\right\rangle, \tag{2}$$

$$\left|\Psi_i^\sigma(t)\right\rangle = \sum_{\vec{n}^\sigma|N_\sigma} C_{i,\vec{n}^\sigma}(t)\,|\vec{n}^\sigma(t)\rangle\,. \tag{3}$$

In the first step [see Eq. (2)], the majority and impurity degrees of freedom x_i and y, respectively, are separated and assigned to $S \in \mathbb{N}$ time-dependent species wave functions $|\Psi_i^\sigma(t)\rangle$. The sum of product form is very convenient as it makes evident the entanglement between the two components. In particular, we use the von Neumann entropy given by $S_{\mathrm{vN}} = -\sum_i \lambda_i \ln(\lambda_i)$ to quantify the degree of entanglement. The time-dependent weights $\lambda_i(t)$ are normalized $\sum_i^S \lambda_i(t) = 1$ and sorted in descending order. A composite system with $\lambda_1(t) \approx 1$ is considered disentangled. Assuming $S = 1$ in the expansion is called a species mean-field (SMF) approximation. In the second step [see Eq. (3)], every species wave function belonging to component σ is expanded in the Fock-state basis $|\vec{n}^\sigma(t)\rangle$ with time-dependent coefficients $C_{i,\vec{n}^\sigma}(t)$. The time dependence of number states is meant implicitly through the time dependence of $s_\sigma \in \mathbb{N}$ underlying SPFs $\varphi_j^\sigma(t)$ which are represented using a harmonic discrete variable representation (DVR) [103,104]. The DVR is an orthonormal set of eigenfunctions of the position operator, represented by a finite analytical orthonormal basis, called DVR basis. The DVR functions act like a delta function within the finite space and provide analytical expressions for matrix representation of kinetic and position operators making their evaluation very efficient. The notation $\vec{n}^\sigma|N_\sigma$ denotes particle-number conservation, i.e., $\sum_i^{s_\sigma} n_i^\sigma = N_\sigma$. Finally, by applying the Dirac-Frenkel variational principle [105] the equations of motion for λ_i, $C_{i,\vec{n}^\sigma}$, and φ_j^σ are obtained. The convergence of ML-X is controlled via S, s_σ, and the number of DVR grid points. We use $S = s_\sigma = 8$ for $N_A = 5$ and $S = s_\sigma = 6$ for $N_A = 10$. The DVR grid spans an interval $[-6, 6]$ and we choose 151 DVR grid points.

B. Compressed sensing analysis

In this work, we aim to extract frequencies $\Omega_{n,m} = E_n - E_m$ of system's excitations where E_n denotes the eigenenergy of the nth eigenvector $|\psi_n\rangle$ of H. Any physical observable $\hat{O}$ carries information about excited eigenstates $\langle\hat{O}\rangle_t = \sum_{n,m} c_m^* c_n \langle\psi_m|\hat{O}|\psi_n\rangle e^{-i\Omega_{n,m}t}$, as long as the transition matrix elements $\langle\psi_m|\hat{O}|\psi_n\rangle$ are nonzero and the corresponding eigenstates are initially populated $c_n c_m \neq 0$ where $c_n = \langle\psi_n|\Psi(t_0)\rangle$. We perform a sampling of breathing observables with a uniform rate Δt over an interval $[0, T]$ containing $T/\Delta t + 1 = N_t$ points. It gives us a finite time signal $\mathbf{f} \in \mathbb{R}^{N_t}$ with components f_j of discrete variable $t_j \in \mathbb{R}$, i.e., $f_j = f(t_j) = f(\Delta t\, j)$ with integer index $j \in [0, N_t - 1] \subset \mathbb{N}_0$.

A straightforward way to retain the frequencies contained in $\mathbf{f}$ is to perform a discrete Fourier transformation (DFT), expressed as a linear map $\mathbf{Af} = \mathbf{g}$ with a square matrix $\mathbf{A} \in \mathbb{C}^{N_t \times N_t}$ and signal's representation in the frequency domain $\mathbf{g} \in \mathbb{C}^{N_t}$. The latter is characterized by frequency spacing $\Delta\omega$ and cutoff frequency ω_{cut}, i.e., it has components $g_j = g(\omega_j) = g(\Delta\omega j)$ of discrete variable $\omega_j \in \mathbb{R}$ and for odd (even) $N_\omega = N_t$ number of points spans an open (closed) interval with end points $-\omega_{\mathrm{cut}}/2$ and $\omega_{\mathrm{cut}}/2$.

The sampling parameters of time and frequency domain are interrelated. Thus, the sampling time T determines the frequency spacing $\Delta\omega = 2\pi/T$, while the sampling rate Δt determines the Nyquist frequency $\omega_{\mathrm{cut}} = \pi/\Delta t$. In principle, frequencies can be retained with arbitrary resolution, if sampled long enough, while highly oscillatory components require a finer sampling rate. In practice, there are technical limitations such as generation, storage, and processing of

data. Given a complex system such as ours, data generation becomes a time-consuming factor, making a good resolution in frequency domain out of reach.

In order to overcome this obstacle, some prior information about signal's properties might become useful. Since the system is perturbed weakly, we expect only the low-energy excitations to be of relevance for the underlying dynamics. In particular, we expect $\mathbf{g}$ to be sparse with major components located in the low-frequency region.

With this prior knowledge, *compressed sensing* (CS) allows to retain the frequencies with a very high resolution while keeping the simulation time with ML-X reasonably small. To this end, we formulate our problem as finding the vector $\mathbf{g}$ satisfying the inverse DFT condition, i.e., $\mathbf{f} = \mathbf{A}^\dagger \mathbf{g}$. However, $\mathbf{A}^\dagger \in \mathbb{C}^{N_t \times N_w}$ is now a rectangular matrix with $N_w \gg N_t$ and $\mathbf{g} \in \mathbb{C}^{N_\omega}$ resulting in an underdetermined system of equations. Here, $\mathbf{A}^\dagger$ is a submatrix of the inverse square DFT matrix $\mathbf{A}^\dagger \in \mathbb{C}^{N_\omega \times N_\omega}$, with the last $N_\omega - N_t$ rows being removed. Importantly, the number of columns N_ω and thus the frequency spacing $\Delta\omega$ can be chosen independently of the simulation time T. Intuitively, this implies that $\mathbf{g}$ has been generated by a signal extended over a larger region $T' > T$ than the current one $\mathbf{f}$, though the information contained beyond T is considered redundant given the priors underlying the evolution.

In order to find a sparse solution to a linear ill-posed inverse problem, we formulate it as $\ell 1$-norm penalized least-squares minimization task known as *basis pursuit denoising* (BPDN) [106]:

$$\min_{\mathbf{g}} \tfrac{1}{2}\|\mathbf{f} - \mathbf{A}^\dagger \mathbf{g}\|_2^2 + \lambda \|\mathbf{g}\|_1, \tag{4}$$

where $\|\mathbf{x}\|_p = (\sum_i |x_i|^p)^{1/p}$ while the penalty term $\lambda \geqslant 0$ controls the tradeoff between the sparsity of the solution and the constraint violation in the presence of noisy signal $\mathbf{f}$. We use the least-angle regression (LARS) [107] minimization algorithm to solve Eq. (4) and perform a mean normalization of the signal $\mathbf{f} \to \tilde{\mathbf{f}} = (\mathbf{f} - \bar{\mathbf{f}})/\|\mathbf{f}\|_1$ beforehand. The employed implementation requires real inputs in Eq. (4). Real $\mathbf{f}$ implies Hermitian $\mathbf{g}$ and we use this symmetry to reformulate $\mathbf{g}$ as a real vector: $\mathbf{g} \to \tilde{\mathbf{g}} \in \mathbb{R}^{2N_\omega} = (\mathrm{Re}(\mathbf{g}), \mathrm{Im}(\mathbf{g}))$. Correspondingly, the inverse Fourier matrix $\mathbf{A}^\dagger \to \mathbf{M} \in \mathbb{R}^{N_t \times 2N_\omega} = (\mathbf{C}, \mathbf{D})$ is now composed of two real submatrices $\mathbf{C} \in \mathbb{R}^{N_t \times N_\omega}$ with components $c_{i,j} = \cos(\epsilon ij)$ and $\mathbf{D} \in \mathbb{R}^{N_t \times N_\omega}$ with components $d_{i,j} = \sin(\epsilon ij)$ where $\epsilon = \Delta t \Delta\omega$. The ML-X time-domain parameters are chosen as $T = 40$ and $\Delta t = 0.05$, whereas the CS frequency-domain parameters are $\omega_{\mathrm{cut}} = 20$ and $\Delta\omega = 0.01$.[1] The only noise our signal has is due to floating point numbers and we decide upon the penalty parameter $\lambda = 10^{-6}$ which displays great performance in terms of accuracy and computation time, which has been tested on a set of randomly generated signals composed of ≈10–20 frequency components.

As input time signals $\mathbf{f}$ we use the expectation values of breathing observables $\sum_i \hat{x}_i^2$ for the majority species and $\hat{y}^2$ for the impurity evaluated with respect to the dynamical state $|\Psi(t)\rangle$ obtained by ML-X. We apply the CS algorithm to obtain the corresponding vector $\tilde{\mathbf{g}}$. Then, we map $\tilde{\mathbf{g}}$ back to $\mathbf{g}$ and convert complex values into amplitudes, i.e., $g_j \to |\mathrm{Re}(g_j) + \mathrm{Im}(g_j)|$. The final vector we call a Fourier power spectrum and label it as $X^2(\omega)$ for the majority component and $Y^2(\omega)$ for the impurity. Finally, for a fixed set of physical parameter values we construct an averaged power spectrum $\Sigma = (X^2 + Y^2)/2$. An example is shown in Fig. 2. Each frequency is classified as being of a majority type (red), an impurity type (blue), or of a mixed type depending on the relative weights of X^2 and Y^2 in Σ. These are encoded in subsequent figures (Figs. 7–10 and 13) as a pie chart of two colors for each breathing frequency. Additionally, we use the transparency to indicate the magnitude of participating breathing modes relative to the most relevant mode of amplitude $\max(\Sigma) = \Sigma_{\max}$ such that faded colors imply less relevant modes. Frequencies with a contribution below $\Sigma_{\max}/10$ are discarded. This amounts to neglecting (i) low-amplitude oscillations among any two eigenstates not involving the reference eigenstate with the largest population, and (ii) numerically introduced "phantom" peaks which are also of minor amplitude. While the amplitude filtering allows us to focus only on major modes participating in the breathing dynamics, it introduces discontinuities in the subsequent figures (Figs. 7–10 and 13). Namely, it causes some modes, usually of a faint color, to "randomly" appear and disappear with increasing g_{AB}. The reason is a fluctuation in the population of eigenstates responsible for these modes resulting in mode amplitude fluctuation around the chosen threshold value.

A last remark is in order. Occasionally, the matrix $\mathbf{M}$ becomes ill conditioned. As a result, the algorithm produces a nonunique solution. Whenever this happens, we obtain either wrong frequencies or correct frequencies but with altered amplitudes. Fortunately, as we monitor the frequency modes continuously as a function of g_{AB} we are able to differentiate between the two cases. In the first case, we manually remove all frequencies at given g_{AB}, while in the second case we may encounter isolated absent data points.

IV. RESULTS

First, in Sec. IV A we summarize results concerning the breathing dynamics of a single particle, a single-component condensate, two distinguishable particles, and a particle-balanced few-body Bose-Bose mixture. This will provide us with useful insights for the interpretation of breathing modes unraveled in the Bose polaron setup being the subject of Sec. IV B. In Sec. IV C we investigate the impact of the trap ratio η on the breathing spectrum accounting for two cases: a "broad" ($\eta < 1$) and a "narrow" ($\eta > 1$) impurity. Finally, in Sec. IV D we study the breathing response of the first excited state having odd global parity and contrast it to the response of the ground state which is of even global parity.

In the following, when all interactions are zero we employ a notation $|\vec{n}\rangle = |n_1, n_2, \ldots\rangle$ to denote n_i particles occupying the ith orbital of a single-particle quantum harmonic oscillator. It is not to be confused with permanents introduced in Sec. III A where the orbitals are variationally optimal at each time instant. We also drop the redundant zeros in the vector tail once all the particles have been accounted for, i.e.,

[1] We remark that similar resolution with DFT can be obtained with $T \approx 600$.

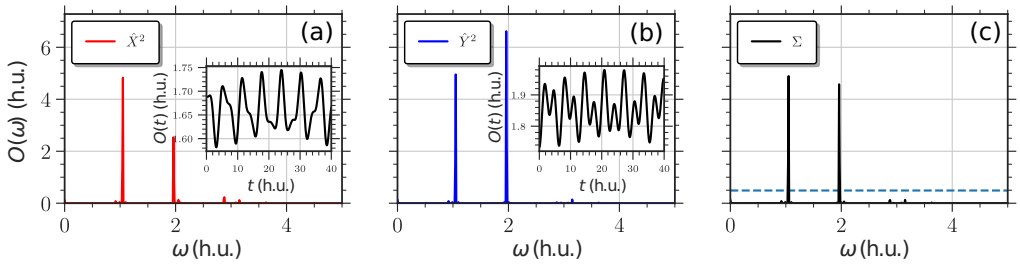

FIG. 2. Fourier power spectrum $X^2(\omega)$ (a) and $Y^2(\omega)$ (b) obtained by applying a compressed sensing algorithm to the expectation values of the breathing observables $\langle\sum_i \hat{x}_i^2\rangle_t$ and $\langle\hat{y}^2\rangle_t$ (insets) evaluated with respect to a dynamical state $|\Psi(t)\rangle$ obtained by the multilayer multiconfiguration time-dependent Hartree method for mixtures. In the averaged power spectrum $\Sigma(\omega)$ (c) the dashed line indicates a threshold magnitude and only frequencies above it are accounted for in Sec. IV (see text). The physical parameters are $\eta = 1, N_A = 5, N_B = 1, g_{AB} = 2.0$, $g_A = 0$ (see Sec. II) and the compressing sensing parameters are $T = 40$, $\Delta t = 0.1$, $\omega_{\text{cut}} = 20$, and $\Delta\omega = 0.01$ (see Sec. III B). All quantities are given in harmonic units.

$\sum_i n_i = N$. The notation $|\vec{n}^A\rangle \otimes |\vec{n}^B\rangle$ denotes a product state for the two components. Note that for unequal traps ($\eta \neq 1$) the orbitals for each species are different.

For Figs. 7–10 and 13 we did a comparison to results obtained from the ML-X method of lower dimension $S = s_\sigma = 6$ ($S = s_\sigma = 4$), for $N_A = 5$ ($N_A = 10$) particles. Instead of displaying the corresponding plots of less converged simulations we put together the most relevant findings for the reader to keep in mind while reading Sec. IV. First, for the values of corresponding frequencies, we evidenced small quantitative discrepancies below ± 0.02 (in harmonic units), being larger for stronger couplings. Second, we observed that the transparency of the modes (mode amplitude) as well as the ratio of pie slices (species correspondence) for each point maintain their overall qualitative behavior.

A. Few-body Bose-Bose mixture

The breathing mode frequency of a single particle confined in a parabolic trap of frequency ω is known to be $\Omega = 2\omega$, corresponding to an excitation by two energy quanta $|0, 0, 1\rangle$ with respect to the harmonic oscillator basis. An ensemble of N noninteracting ($g = 0$) bosonic particles introduces an additional eigenstate of the same excitation energy 2ω, namely, a two-particle excitation $|N - 2, 2\rangle$ being degenerate with $|N - 1, 0, 1\rangle$. For interacting particles, the degeneracy is lifted. The frequency of one mode remains constant for any g and relates to the c.m. breathing motion. The frequency of the other mode is highly sensitive to a variation of g and characterizes the relative motion of particles [77,108]. A mean-field ansatz for the breathing dynamics, being a single-particle picture, is able to recover only the interaction-sensitive breathing frequency, though with quantitative deviations as compared to an exact solution, especially at sizable interactions.

1. $1 + 1$ *mixture*

The Hamiltonian (1) can be solved analytically for $N_A = 1$ and $N_B = 1$ at $\eta = 1$. To this end, we perform a coordinate transformation to the relative frame composed of the center of mass $R = (x + y)/2$ and relative $r = x - y$ coordinates. In this frame, the two degrees of freedom decouple $H = H_R + H_r$.

The first term H_R is a quantum harmonic oscillator of mass $m_R = 2$:

$$H_R = -\frac{\partial^2}{4\partial R^2} + R^2. \tag{5}$$

The solutions $\Phi_k(R; m_R)$ are the well-known Hermite functions

$$\Phi_k(z; m) = \frac{1}{\sqrt{2^n n!}}\left(\frac{m}{\pi}\right)^{1/4} \exp\left(-\frac{mz^2}{2}\right) H_n(\sqrt{m}z) \tag{6}$$

with m the particle mass and H_n the physicists' Hermite polynomials. The corresponding eigenenergies are $\epsilon_k = k + \frac{1}{2}$.

The second term H_r is a quantum harmonic oscillator of mass $m_r = \frac{1}{2}$ with a delta constraint:

$$H_r = -\frac{\partial^2}{\partial r^2} + \frac{1}{4}r^2 + g\delta(r), \tag{7}$$

where we substituted $g_{AB} \to g$ to simplify the notation. The solutions can be classified by parity:

$$\phi_l(r) = \begin{cases} D_{\mu(g,l/2)}(r), & l \text{ even} \\ \Phi_l(r; m_r), & l \text{ odd.} \end{cases} \tag{8}$$

The even parity states are the symmetrized parabolic cylinder functions

$$D_\mu(z) = \sqrt{2^\mu} \exp\left(-\frac{z^2}{4}\right) U\left(-\frac{1}{2}\mu, \frac{1}{2}, \frac{1}{2}z^2\right) \tag{9}$$

with $U(a, b, z)$ denoting the Tricomi's hypergeometric function and $\mu(g, l/2)$,[2] being a real-valued quantum number obtained by solving a transcendental equation

$$g = -2^{\frac{3}{2}} \frac{\Gamma\left(\frac{1-\mu}{2}\right)}{\Gamma\left(-\frac{\mu}{2}\right)}, \tag{10}$$

which for a fixed g gives a ladder of solutions and $l/2$ refers to the index number. The corresponding eigenenergies are $\epsilon_l = \mu(g, l/2) + \frac{1}{2}$. The odd parity states vanish at $r = 0$ and thus

[2] $l < \mu(g, l/2) < l + 1$ for $0 < g < \infty$.

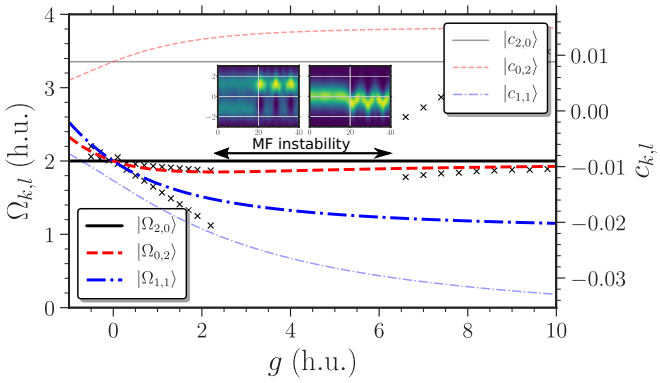

FIG. 3. Breathing mode frequencies (opaque lines) $\Omega_{k,l} = E_{k,l} - E_{0,0}$ [see Eq. (11)] of two distinguishable particles $N_A = 1$ and $N_B = 1$ as a function of the coupling $g_{AB} \equiv g$ at equal trapping frequency ratio $\eta = 1$. Population amplitudes (transparent lines) $c_{k,l}$ [see Eq. (13)] of eigenstates $|\psi_{k,l}\rangle$ upon quenching the ground state $|E_0\rangle_{\eta_0}$ from $\eta_0 = 1.05$ to $\eta = 1$. Crosses stand for frequencies extracted from a laboratory frame mean-field ansatz. Inset: representative example of dynamical symmetry breaking in the one-body densities $\rho_1(x,t)$ (left) and $\rho_1(y,t)$ (right) at $2.5 < g < 6.5$ occurring for a mean-field ansatz. All quantities are given in harmonic units.

do not experience the delta barrier. They are the odd parity Hermite functions $\Phi_l(r; m_r)$ of mass m_r and eigenenergy $\epsilon_l = l + \frac{1}{2}$.

The two-body eigenstate becomes a product state $\psi_{k,l}(R,r) = \Phi_k(R; m_R)\phi_l(r)$ with total energy:

$$E_{k,l} = \begin{cases} k + \mu(g, l/2) + 1, & l \text{ even} \\ k + l + 1, & l \text{ odd.} \end{cases} \tag{11}$$

Having analytical expressions for the eigenstates, we proceed with the breathing dynamics induced by releasing the trap of the second particle slightly from $\eta_0 = 1.05$ to $\eta = 1$. The time evolution of the prequench ground state $|E_0\rangle_{\eta_0}$ can be expressed in terms of postquench eigenstates $|\psi_{k,l}\rangle$:

$$|E_0\rangle_{\eta_0} = \sum_{k,l} c_{k,l} e^{-iE_{k,l}t} |\psi_{k,l}\rangle . \tag{12}$$

To find the occupancy of eigenstates $c_{k,l} = \langle \psi_{k,l}|E_0\rangle_{\eta_0}$ we perform first-order perturbation theory for the ground state:

$$c_{k,l} = \Delta\eta \frac{\langle \psi_{k,l}|y^2|\psi_{0,0}\rangle}{\Omega_{k,l}}, \tag{13}$$

with $\Delta\eta = \eta_0 - \eta$ and $\Omega_{k,l} = E_{k,l} - E_{0,0}$. The coupling operator $y^2 = R^2 - Rr + r^2/4$ can populate states $|\psi_{2,0}\rangle$ via R^2, $|\psi_{0,2}\rangle$ via r^2, and $|\psi_{1,1}\rangle$ via Rr. All these states are of even global parity, $|\psi_{2,0}\rangle$ and $|\psi_{0,2}\rangle$ are of even c.m. parity, and $|\psi_{1,1}\rangle$ is of odd c.m. parity. They have the same energy gap $\Omega_{k,l} = 2$ with respect to the ground state at $g = 0$. We call them the *first-order* breathing manifold.[3]

In Fig. 3 we display the energy gaps (opaque curves) as a function of g (cf. also Fig. 8 in [76]). We concentrate on the three eigenstates from the first breathing manifold. At $g = 0$ they are degenerate with excitation energy $\Omega = 2$. In the laboratory frame, these are a single-particle excitation by two energy quanta in either of the components, i.e., $|0,0,1\rangle \otimes |1\rangle$ and $|1\rangle \otimes |0,0,1\rangle$, as well as a two-particle excitation $|0,1\rangle \otimes |0,1\rangle$. The latter can be thought of as a "correlated" sloshing excitation: $\langle X\rangle = \langle Y\rangle = 0$ and $\langle XY\rangle \neq 0$. Below we will reveal what kind of motion the particles actually undergo.

When the interaction strength g becomes nonzero, we employ the relative frame. The degenerate manifold splits at finite g. The frequency of the c.m. mode $|\psi_{2,0}\rangle$ is independent of interactions $\Omega_{2,0} = 2$ (black solid opaque line). The relative motion mode $|\psi_{0,2}\rangle$ features an interaction-sensitive frequency $\Omega_{0,2} = [\mu(g,1) - \mu(g,0)]$ (red dashed opaque line), which displays a single minimum at positive g, is monotonically decreasing function of g left of this minimum, and saturates as $g \to \infty$. Curves with such behavior will be abbreviated as *single turning point* (STP) curves. Actually, all mode frequencies will saturate at large positive g because of contact interaction: the eigenenergies are monotonically increasing functions of g,[4] and are bounded from above due to hard-core repulsion.[5] The hybrid "sloshing" mode $|\psi_{1,1}\rangle$ has a frequency $\Omega_{1,1} = [2 - \mu(g,0)]$ (blue dashed-dotted opaque line) which is a monotonically decreasing function of g. It saturates to a frequency $\Omega = 1$ at very large positive couplings matching the interaction-independent sloshing (dipole) mode frequency of a single-component condensate in a harmonic trap [52].

Thus, distinguishability allows for an additional breathing mode. A laboratory-frame mean-field ansatz (crosses) predicts two interaction-sensitive breathing frequencies though neither of the exact modes is matched quantitatively for all g. Importantly, the monotonically decreasing frequency can be matched only at very weak interactions, implying the relevance of entanglement in multicomponent mixtures. There is even a region of interactions $2.5 < g < 6.5$, where dynamical symmetry breaking takes place, i.e., the parity symmetry becomes violated after some propagation time (see the inset). It starts right after the low-frequency mean-field mode has reached the value $\Omega = 1$ around $g \approx 2.5$, being the limiting value of the exact mode $|\psi_{1,1}\rangle$ at $g = \infty$.

What kind of motion does each mode induce? In the relative frame, the one-body densities $\rho_1(R,t)$ and $\rho_1(r,t)$ undergo the following evolution:

$$\rho_1(R,t) \approx c_{0,0}^2 \rho_1^{(0,0)}(R) + 2\textstyle\sum_{k,l} c_{0,0} c_{k,l} \rho_1^{(k,l)}(R) \cos(\Omega_{k,l} t),$$

$$\rho_1(r,t) \approx c_{0,0}^2 \rho_1^{(0,0)}(r) + 2\textstyle\sum_{k,l} c_{0,0} c_{k,l} \rho_1^{(k,l)}(r) \cos(\Omega_{k,l} t)$$

with the time-independent background densities $\rho_1^{(0,0)}(R)$ and $\rho_1^{(0,0)}(r)$, modulation densities $\rho_1^{(k,l)}(R) = \int dr\, \rho_2^{(k,l)}(R,r)$ and $\rho_1^{(k,l)}(r) = \int dR\, \rho_2^{(k,l)}(R,r)$, where $\rho_2^{(k,l)}(R,r) =$

[3] The nth-order breathing manifold has an energy gap $2n$ with respect to the ground state at $g = 0$.

[4] $\partial E_j / \partial g_{AB} = \int \rho_2^{AB}(z,z)\, dz \geqslant 0$ with $\rho_2^{AB}(z)$ being the diagonal of the reduced intercomponent two-particle density obtained from the many-body eigenstate $|E_j(g_{AB})\rangle$.

[5] $\rho_2^{AB}(z,z) \to 0$ as $g_{AB} \to \infty$.

$\psi_{0,0}(R,r)\psi_{k,l}(R,r)$. We neglected terms $c_{i,j}c_{k,l}$ related to oscillations among the excited states. Inserting the occupied eigenstates we mentioned previously, we get

$$\rho_1(R,t) = c_{0,0}^2\Phi_0^2(R) + 2c_{0,0}c_{2,0}\Phi_0(R)\Phi_2(R)\cos(2t),$$
$$\rho_1(r,t) = c_{0,0}^2\phi_0^2(r) + 2c_{0,0}c_{0,2}\phi_0(r)\phi_2(r)\cos([\mu(g,1) - \mu(g,0)]t).$$

Thus, $\rho_1(R,t)$ performs a constant frequency ($\Omega_{2,0} = 2$) breathing oscillation, while $\rho_1(r,t)$ undergoes an interaction-dependent single-frequency ($\Omega_{0,2} = [\mu(g,1) - \mu(g,0)]$) modulation.

The state $|\psi_{1,1}\rangle$ and the related frequency ($\Omega_{1,1} = [2 - \mu(g,0)]$) are not represented in the reduced "one-body" quantities of the relative frame and can be only revealed on the "two-body" level. In particular, R and r do not perform a sloshing motion, i.e., $\langle R\rangle = \langle r\rangle = 0$ which implies $\langle x\rangle = \langle y\rangle = 0$. Instead, $\langle Rr\rangle = A\cos([2 - \mu(g,0)]t)$ with amplitude $A = 2c_{0,0}c_{1,1}\iint dR\,dr\,Rr\rho_2^{(1,1)}(R,r)$.

What is the imprint of the individual oscillatory term $\rho_2^{(k,l)}(R,r)\cos(\Omega_{k,l}t)$ of the relative frame density matrix $\rho_2(R,r,t)$ describing the two-particle evolution on the reduced one-particle density $\rho_1(x,t)$ of the laboratory frame? To this end, we transform $\rho_2^{(k,l)}(R,r)$ to the laboratory frame and integrate over the coordinate y to get $\rho_1^{(k,l)}(x)$. The corresponding modulations are shown in Fig. 4. Figure 4(a) demonstrates the time-independent background density $\rho_1^{(0,0)}(x)$. At negative g (dotted) it is a narrow Gaussian, which broadens with increasing g (solid) until it finally splits into a two-hump configuration (dashed) indicating that phase separation has taken place. Figure 4(b) is a density modulation (at $t = 0$) stemming from the c.m. breathing $\rho_2^{(2,0)}(R,r)\cos(\Omega_{2,0}t)$. The exact shape is very sensitive to g variation and in particular to the two-hump structure of the background density at $g = 8$ where it develops additional nodes. The dotted and solid curves are typical shapes responsible for the breathing motion of a Gaussian background. The dashed curve ($g = 8$) induces breathing for each individual hump of the background density. Figures 4(c) and 4(d) are density modulations (at $t = 0$) stemming from relative motion breathing $\rho_2^{(0,2)}(R,r)\cos([\mu(g,1) - \mu(g,0)]t)$ and hybrid sloshing $\rho_2^{(1,1)}(R,r)\cos([2 - \mu(g,0)]t)$. For a Gaussian background they produce breathing, while for a two-hump profile we expect a simultaneous outwards and inwards sloshing of the two humps. Both the magnitude and functional behavior of the modulations are robust to g variation. The second particle $\rho_1(y,t)$ does exactly the same, except $\rho_1^{(1,1)}(y,t)$ is inverted, i.e., it has a phase shift of π.

To summarize, two distinguishable particles feature an additional breathing mode in contrast to two indistinguishable particles. The responsible eigenstate has even global parity, though it is of odd center-of-mass parity and odd relative parity. It relates to a hybrid sloshing: $\langle Rr\rangle \neq 0$ while $\langle R\rangle = \langle r\rangle = 0$. It induces a breathing oscillation of the one-body densities though they have a relative phase shift of π. The related mode frequency is a monotonically decreasing function of the interparticle interaction g and a mean-field ansatz fails to capture its functional behavior except for a linear trend at very weak interactions.

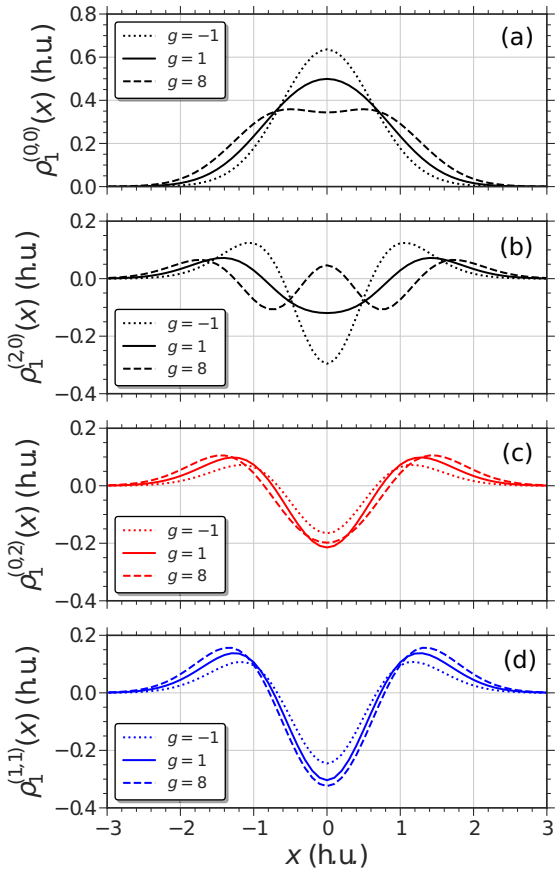

FIG. 4. Decomposition of the one-body density $\rho_1(x)$: (a) time-independent background and time-dependent single-frequency modulations $\rho_1^{(k,l)}(x)$ induced by (b) center-of-mass breathing $\rho_2^{(2,0)}$, (c) interparticle distance breathing $\rho_2^{(0,2)}$, and (d) hybrid sloshing $\rho_2^{(1,1)}$ at different interaction strength g. All quantities are given in harmonic units.

2. 2 + 2 *mixture*

A noninteracting two-component mixture features in total five eigenstates which are two energy quanta above the ground state: two single-particle excitation states $|N_A - 1, 0, 1\rangle \otimes |N_B\rangle$ and $|N_A\rangle \otimes |N_B - 1, 0, 1\rangle$, two states having two indistinguishable particles excited $|N_A - 2, 2\rangle \otimes |N_B\rangle$ and $|N_A\rangle \otimes |N_B - 2, 2\rangle$, and, finally, a state where one particle in each component is excited $|N_A - 1, 1\rangle \otimes |N_B - 1, 1\rangle$. The interactions will (partially) break this manifold of degenerate eigenstates. Each of these states, once populated in the initialization step, will induce a breathing oscillation of a characteristic frequency. Together they represent a first-order breathing manifold.[6] To get an insight how the respective frequencies behave depending on the system's interactions, we briefly summarize and complement the results obtained in [88]. For a few-body fermionic mixture see also [76].

[6]A breathing mode is said to be of nth order if its frequency can be traced to a value $2\omega_\sigma n$ when adiabatically tuning all the interactions to zero.

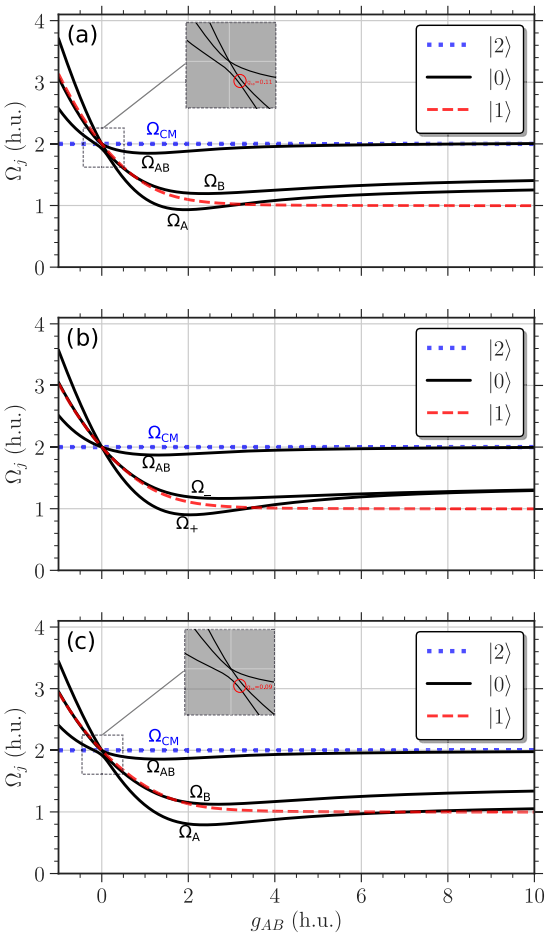

FIG. 5. Energy gaps $\Omega_j = E_j - E_0$ (with respect to the ground state $|E_0\rangle$) of a few-body bosonic mixture $N_A = 2$ and $N_B = 2$ as a function of the intercomponent coupling g_{AB} at equal trapping frequency ratio $\eta = 1$, intracomponent interaction strength $g_B = 0$ for the second component and (a) $g_A = -0.5$, (b) $g_A = 0$, (c) $g_A = 0.5$ for the first component. Whether the corresponding eigenstates are actually excited depends on the quench protocol. Different colors (line styles) refer to the center-of-mass (c.m.) quantum number in the eigenstate $|E_j\rangle$. The c.m. is a decoupled degree of freedom in this harmonic confinement. The insets represent a zoom-in on regions with avoided crossings which are indicated by circles and caused by $g_A \neq g_B$ asymmetry. Curves of different colors (line styles) may only cross. All quantities are given in harmonic units.

In [88], each component consists of two particles trapped within the same parabolic confinement $\eta = 1$. Both components experience a sudden but weak trap quench of the same magnitude and the system's response is studied for different intracomponent and intercomponent interaction strengths. Importantly, the c.m. motion decouples while the quench operator prevents transitions among eigenstates possessing different c.m. parity. By performing an exact diagonalization method based on a correlated basis (see [88] for more details)[7] up to four breathing mode frequencies have been identified and analyzed. These are reproduced in Fig. 5 as a function of the intercomponent coupling g_{AB} for three different intracomponent interaction values g_A [Figs. 5(a)–5(c)], assuming $g_B = 0$. The curve colors (line styles) encode the c.m. quantum number of the responsible eigenstates $|E_j\rangle$, while the reference state $|E_{\text{ref}}\rangle$ is the ground state $|E_0\rangle$ of even c.m. parity.

The blue dotted curve is a double excitation of the c.m. harmonic oscillator, the $\Omega_{\text{c.m.}}$ mode. Thus, it is independent of interactions g_A, g_B, and g_{AB}. The three black solid curves are interaction-sensitive relative motion modes. They have been labeled Ω_+, Ω_- (Ω_A, Ω_B) for species-(anti)symmetric parameter choice, i.e., $g_A = g_B$ ($g_A \neq g_B$), and Ω_{AB}. All of them are STP curves. The Ω_{AB} mode is quite shallow, weakly affected by intracomponent interactions and degenerates with $\Omega_{\text{c.m.}}$ at strong coupling g_{AB}. The two lower ones are very sensitive to intracomponent interactions and, depending on the presence of the species-exchange symmetry,[8] they either intersect or experience a bending in the vicinity of avoided crossings [Figs. 5(a) and 5(c) at $g_{AB} \approx 0$].

Thus, for a weak *species-symmetric* trap quench, the system features 2–4 of the above-mentioned breathing frequencies depending on the strength of interaction parameters. For a weak *species-asymmetric* trap quench, all the above-mentioned modes are still energetically accessible plus one extra mode of a comparable frequency. Indeed, based on our discussion on the 1+1 mixture, we anticipate an eigenstate with odd c.m. parity and even global parity to eventually contribute to the dynamics. The corresponding breathing mode frequency is represented by the red dashed curve in Fig. 5. We observe again a monotonous decrease of the mode frequency with increasing coupling g_{AB} until it energetically separates from one of the relative modes at $g_{AB} \approx 1$ and, finally, saturates to a value of 1.0 at $g_{AB} \geqslant 4$. Its frequency is barely affected by g_σ. Interestingly, the mode is again invisible to numerical approaches which ignore the entanglement as we evidence by comparing a numerically exact solution to a SMF ansatz.

B. Few-body Bose polaron

Now we turn our attention to a single impurity $N_B = 1$ in a few-body majority environment having $N_A = 5$ or 10 particles. In contrast to [88], here, we initiate the breathing dynamics by relaxing only the B component, while the A component is affected indirectly via the intercomponent coupling g_{AB}. Representative breathing motions in each component can be seen in Fig. 6. At $\eta = 1$ the c.m. motion still decouples from the relative motions. In particular, the quench operator may mediate between eigenstates of different c.m. parity inducing eventually a special breathing mode caused by population of an eigenstate with odd c.m. parity. Furthermore, there is only one particle in the B component. Thus, a double excitation state $|N_A\rangle \otimes |N_B - 2, 2\rangle$ (see Sec. IV A) does not exist and we expect that one of the relative modes (black solid curves in Fig. 5), whose frequency is notably affected by interactions, will not be present.

[7] It can be applied to bosonic mixtures of $N_A \leqslant 2$ and $N_B \leqslant 2$ particles subject to contact interactions in a 1D harmonic trap.

[8] Corresponding to a map $x_i \mapsto y_i$ at $g_A = g_B$.

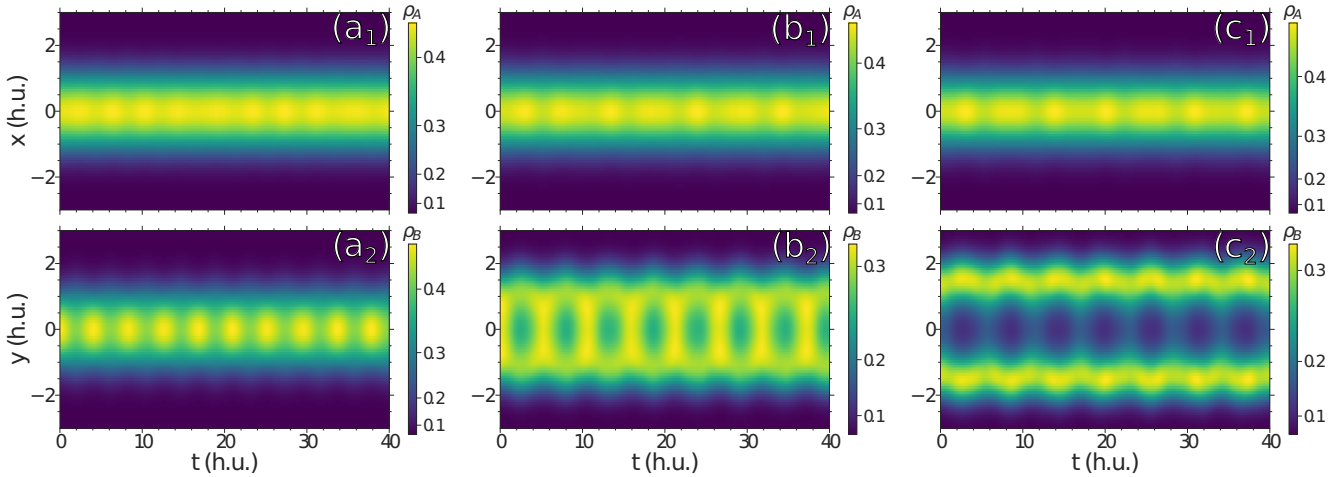

FIG. 6. Breathing oscillations of the one-body densities of the majority component $\rho_1^A(x)$ (first row) and the impurity $\rho_1^B(y)$ (second row) at a fixed majority-component interaction $g_A = 0.5$ for $N_A = 5$ and $N_B = 1$ particles initiated by preparation of the ground state of even global parity followed by an abrupt change of the trap ratio from $\eta = 1.05$ to 1. Columns 1–3 correspond to different intercomponent couplings: (a) $g_{AB} = 0.5$, (b) $g_{AB} = 1.0$, and (c) $g_{AB} = 1.5$. Note that the initial state displays the onset of phase separation in (b) and a pronounced core-shell phase in (c). All quantities are given in harmonic units.

In Figs. 7 and 8 we show the excitation spectrum of the breathing dynamics initialized by quenching the equilibrated system at trap ratio $\eta = 1.05$ to 1, i.e., partially releasing the trap of the impurity. The majority component consists of $N_A = 5$ (Fig. 7) or $N_A = 10$ (Fig. 8) particles subject to several different majority component interactions g_A [Figs. 7(a)–7(c) and 8(a)–8(c)]. Only frequencies of modes whose contribution is above 10% of the maximum amplitude $\Sigma_{\max}$ in the averaged power spectrum are shown. Additionally, each frequency data point (full circle) is represented as a pie chart of two different colors and encodes the contribution of the breathing observables to the averaged power spectrum (see Sec. III B): blue color for the impurity $\hat{y}^2$ and red color for the majority component $\sum_i \hat{x}_i^2$. The decomposition into colors tells us whether the respective mode is a single-species mode or whether it is of a mixed character and to what extent. Furthermore, the color intensity indicates the participation of the respective mode in the breathing dynamics as compared to the most relevant mode at fixed g_{AB} (a more intense color indicates a stronger contribution). Finally, the crosses represent frequencies of modes excited by the same procedure but numerically ignoring the entanglement in the initial state and the subsequent dynamics (SMF approximation).

Let us first focus on Fig. 7(b), the case of a noninteracting majority species ($g_A = 0$). At $g_{AB} = 0$ only the impurity is excited (blue circle) performing a breathing motion with frequency $\Omega = 2$ as expected. As one increases the coupling strength ($g_{AB} > 0$), a second mode of decreasing frequency emerges resulting in a beating. This mode has the largest contribution to the ongoing dynamics and is of a mixed type, i.e., it appears both in the majority and impurity breathing observables. For the latter reason it can correspond to the Ω_{AB} mode of even c.m. parity or to the hybrid sloshing mode of odd c.m. parity we introduced in the previous section. The quench operator can mediate among eigenstates of different c.m. parity so both are allowed to be populated. Considering limited frequency resolution and the possibility of a quasidegeneracy of the red (dashed) mode with a black (solid) mode observed in Fig. 5, it is likely that the observed mode gets a contribution from both eigenstates. For that reason, no particular eigenstate label can be assigned to it. The frequency of the other mode experiences only a slight variation $\Omega \approx 2$. It is represented to a larger extent in the majority component, has a minor amplitude, and is reproduced by a SMF ansatz. Thus, we assign it to the Ω_A mode encountered in Sec. IV A (cf. black curves in Fig. 5), though here it is less sensitive to g_{AB} variation, supposedly due to the particle-number imbalance.

Around $g_{AB} \approx 0.75$ the lower frequency splits into two branches of comparable significance, resulting altogether in three modes. One of the emerging branches possesses a continuously decreasing frequency with increasing g_{AB} approaching the value $\Omega = 1$. It matches the description of the hybrid sloshing mode which was emphasized in Sec. IV A (cf. red dashed curve in Fig. 5). Interestingly, it is equally represented in both subsystems despite the particle-number imbalance and quench asymmetry. The other frequency branch bends and starts recovering towards $\Omega = 2$ with increasing g_{AB} while gradually becoming a pure signature of the impurity motion only (the blue slice dominates at $g_{AB} = 2$). It matches the functional behavior of the Ω_{AB} mode (STP curve) mentioned in Sec. IV A (cf. the black solid curves in Fig. 5).

At weak negative coupling ($g_{AB} < 0$) one observes also a beating behavior, although here both frequencies are increasing with decreasing g_{AB}. The dominant frequency in the power spectrum is more sensitive to the coupling variation, is of a mixed type and reproducible by a SMF ansatz (Ω_{AB} mode), while the second is barely affected and primarily represented in the majority component (Ω_A mode). Below a certain threshold ($g_{AB} < -0.4$) one observes low-amplitude traces of a third frequency.

We discover several major alternations in the excitation spectrum when the majority component becomes interacting. For weakly attractive ($g_A = -0.5$) majority particles in Fig. 7(a) the coupling-insensitive mode frequency is seem-

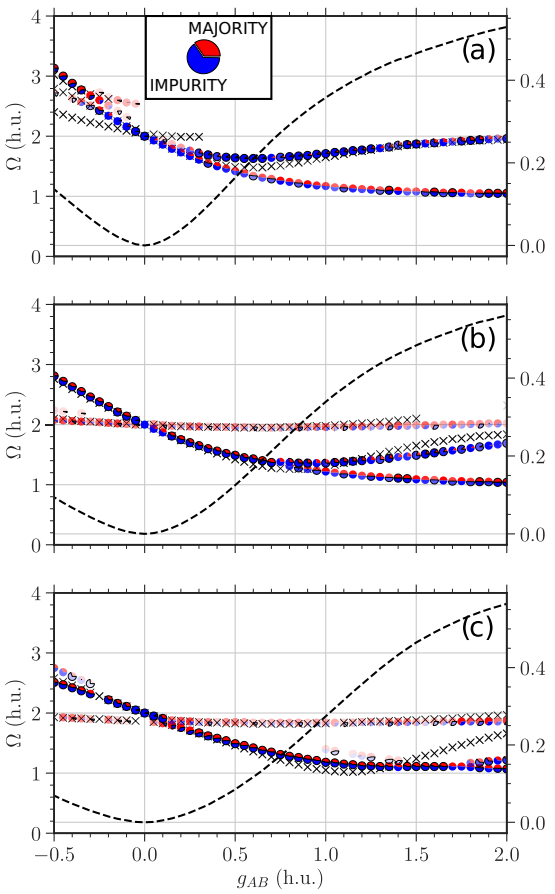

FIG. 7. Frequencies Ω of breathing modes excited by quenching the ground state $|E_0\rangle$ of the Bose polaron for $N_A = 5$ and $N_B = 1$, meaning a change in the trap ratio from $\eta = 1.05$ to 1.0, shown as a function of the intercomponent coupling g_{AB} for a fixed majority component interaction (a) $g_A = -0.5$, (b) $g_A = 0$, and (c) $g_A = 0.5$. Each frequency data point (full circle) is divided into two sectors (of different colors) representing the contribution of the breathing observables $\langle \sum_i \hat{x}_i^2 \rangle_t$ or $\langle \hat{y}^2 \rangle_t$ to the averaged power spectrum Σ at that frequency (see Sec. III B). The corresponding color intensity indicates the relative strength with respect to the maximum amplitude $\Sigma_{\max}$ in the averaged power spectrum for fixed g_{AB} and only modes with contribution above 10% of $\Sigma_{\max}$ are presented. Crosses stand for frequencies of modes excited within the SMF approximation. Black dashed line indicates the entanglement entropy S_{vN} of the initial state. All quantities are given in harmonic units.

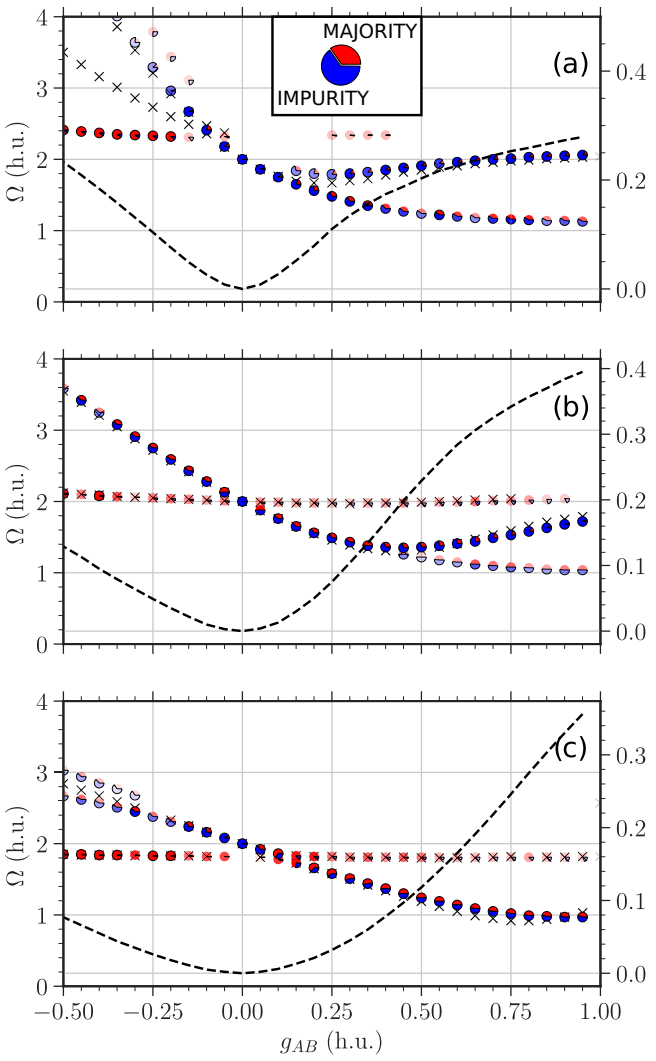

FIG. 8. Same as in Fig. 7 but for $N_A = 10$. All quantities are given in harmonic units.

ingly absent. At positive increasing g_{AB} the bifurcation of the continuously decaying frequency takes place already for a very weak coupling strength ($g_{AB} \approx 0.1$). It can be related to the fact that the phase separation also takes place at weaker couplings. The character of the excited modes is mostly the same as for $g_A = 0$. At negative decreasing g_{AB} we observe an emerging multifrequency breathing composed of three modes. The lower-frequency mode loses amplitude in favor of higher-frequency modes ($-0.4 < g_{AB} < -0.1$). Then it turns into a single-frequency breathing ($g_{AB} < -0.4$) affecting both components in a similar way.

For weakly repulsive ($g_A = 0.5$) majority particles in Fig. 7(c) the coupling-insensitive mode frequency is still present though energetically shifted downwards to $\Omega = 1.9$. The respective mode is weakly represented in the overall dynamics and affects mainly the majority component. The sensitivity to g_A is yet another indicator that this is the Ω_A mode. The point of bifurcation in the lower-frequency branch is located at a stronger coupling $g_{AB} \approx 1.8$. Phase separation takes place also at stronger couplings which supports our previous conjecture. At negative g_{AB} below a certain threshold ($g_{AB} < -0.3$) a third mode is excited. In contrast to $g_A = 0$, this additional mode is rather manifested in the impurity breathing and has a larger frequency. In summary, the majority component interaction g_A determines the coupling value at which the bifurcation takes place as well as the offset of the coupling-insensitive frequency and whether it can be addressed by the current quench protocol.

Next, we double the number of majority component atoms to get an idea of how it affects the excitation spectrum. In the following, we compare the corresponding subfigures of Figs. 7 and 8. We note that at $N_A = 10$ the interval of the

considered couplings is $g_{AB} \in [-0.5, 1.0]$ as the convergence is more challenging to achieve beyond $g_{AB} > 1$. At $g_A = 0$ [Fig. 8(b)] the bifurcation point is located at a smaller value of g_{AB} compared to the $N_A = 5$ case [see Fig. 7(b)]. Increasing the particle-number imbalance accelerates the phase separation [49]. The coupling-insensitive Ω_A mode frequency is barely affected by the particle-number imbalance.

At $g_A = -0.5$ [Fig. 8(a)] and positive g_{AB} the minimum of the Ω_{AB} frequency mode is shifted to larger frequencies and smaller values of the coupling g_{AB}. The frequency value recovers back to $\Omega = 2$ more quickly already at $g_{AB} \approx 0.75$. The coupling-insensitive Ω_A mode becomes visible at negative g_{AB} and even dominates the breathing dynamics, although the amplitude decays considerably towards $g_{AB} = 0$ and there are only minor traces left at positive coupling ($0.25 < g_{AB} < 0.4$). It is certainly present in the breathing dynamics at positive g_{AB}, but the contribution is not significant enough to overcome the set threshold. The respective frequency is shifted to $\Omega \approx 2.4$. At $g_A = 0.5$ [Fig. 8(c)] the frequency of the coupling-insensitive Ω_A mode experiences a slight shift downwards. At negative g_{AB} it gains amplitude with decreasing g_{AB} until it becomes a dominant mode below $g_{AB} \leqslant -0.25$. The bifurcation point at positive g_{AB} is unfortunately not visible within the covered g_{AB} interval.

Lastly, we want to emphasize the importance of entanglement in our Bose polaron setup. To this end, we neglect it both in the initial state and in the subsequent dynamics (crosses in Figs. 7 and 8). The first striking observation is that in the SMF case, at most *two* frequencies can be extracted. The mode we are missing from the exact simulations is the one whose frequency is a monotonically decreasing function of g_{AB}, making appearance at finite positive g_{AB}. We call a mode, which is not reproducible by a SMF ansatz, an entanglement-sensitive mode. It can be assigned to the eigenstate of odd c.m. parity, also called hybrid "sloshing" mode. Regarding the persistent modes, the Ω_A mode with coupling-insensitive frequency is overall well captured by the species mean-field ansatz, although it tends to overestimate the frequency for large positive values of g_{AB}. The Ω_{AB} mode, whose frequency is STP function of g_{AB}, in general is not well matched by SMF ansatz either mispredicting the location [Fig. 7(c)] or the exact value [Fig. 7(a)] of the minimum. Even if both the location and the value of the minimum are well matched [Fig. 7(b)] there is an increasing discrepancy for strong positive g_{AB}. For a larger particle number (Fig. 8), the consistency between approximated and exact frequencies is much better, though here also we have a mode not reproducible by a SMF ansatz featuring the same functional behavior.

To summarize, we are able to excite up to three breathing modes in the Bose polaron setup by quenching only the impurity. First, there is a coupling-insensitive Ω_A majority mode. Its frequency can be manipulated by the particle-number imbalance or the majority component interaction. Second, there is a monotonically decreasing frequency making appearance at finite positive g_{AB} and converging towards $\Omega = 1.0$ with increasing g_{AB}. It cannot be described by the species mean-field ansatz and matches the functional behavior of the hybrid sloshing mode encountered in the $1 + 1$ and $2 + 2$ mixtures. Third, we have a large-amplitude Ω_{AB} mode which is of a mixed type. The mode frequency is STP function of g_{AB} with a minimum being sensitive to g_A and N_A.

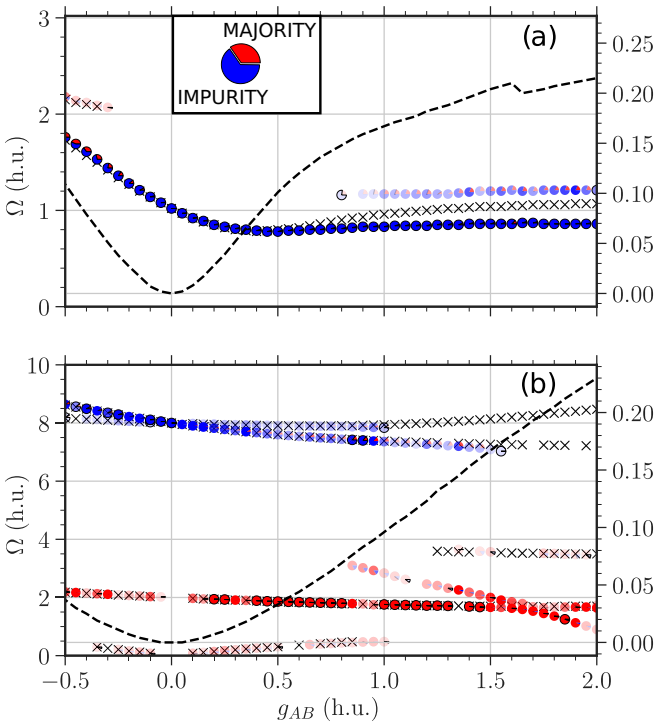

FIG. 9. Frequencies Ω of breathing modes for $N_A = 5$ and $N_B = 1$ as a function of the intercomponent coupling g_{AB} at fixed majority component interaction $g_A = 0$. The trap ratio is quenched in (a) from $\eta = 0.536$ to 0.51 and in (b) from $\eta = 4.2$ to 4. Color coding according to Fig. 7. Black dashed line indicates the entanglement entropy S_{vN} of the initial state. All quantities are given in harmonic units of the majority component.

C. Impact of the trap

Let us now focus on the impact of the external trap, more specifically we consider a situation where the length scale of the impurity $l_B = \sqrt{1/\eta}$, set by the parabolic trap, is either broader ($l_B = 1.4$) or narrower ($l_B = 0.5$) in the postquench system. The quench strength is still 5% of the original trap parameter.

We start with the case of a "broad" impurity $\eta = 0.51$. In Figs. 9(a) and 10(a) we show the breathing spectrum for $N_A = 5$ and 10 majority atoms, respectively. To gain an intuitive picture we set $g_A = 0$. For the decoupled case $g_{AB} = 0$, the lowest-frequency mode is caused by the eigenstate $|N_A\rangle \otimes |0, 0, 1\rangle$, corresponding to a standard breathing of the impurity at frequency $\Omega = 1.02$. It is the only mode excited. Once coupled ($g_{AB} \neq 0$), several other eigenstates may become populated leading to additional breathing modes. The states in question can be continuously traced back to the low-energy eigenstates of a decoupled impurity. First, we have the state $|N_A - 1, 1\rangle \otimes |0, 1\rangle$ corresponding to a hybrid sloshing mode at frequency $\Omega = 1.51$. Then follows a quasidegenerate manifold of three modes: two majority component modes at the same frequency $\Omega = 2$ caused by $|N_A - 1, 0, 1\rangle \otimes |1\rangle$ and $|N_A - 2, 2\rangle \otimes |1\rangle$, and a second order breathing of the

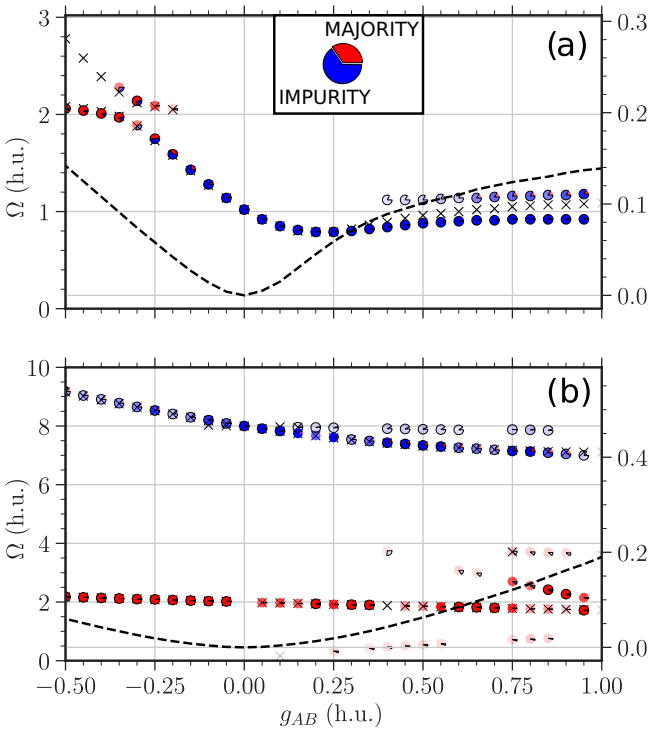

FIG. 10. Same as in Fig. 9 but for $N_A = 10$. All quantities are given in harmonic units of the majority component.

impurity at frequency $\Omega = 2.04$ mediated by $|N_A\rangle \otimes |0, 0, 0, 0, 1\rangle$. Any higher-frequency modes are unlikely to be involved.

At weak coupling g_{AB} there is only one relevant mode excited. It originates from the state $|N_A\rangle \otimes |0, 0, 1\rangle$ and is barely detectable in the majority component breathing. The corresponding frequency is STP function of g_{AB} with a minimum at $g_{AB} \approx 0.5$ for $N_A = 5$ [Fig. 9(a)] and at $g_{AB} \approx 0.25$ for $N_A = 10$ [Fig. 10(a)]. At strong positive g_{AB}, a beating behavior emerges. The amplitude of the additional mode increases gradually with increasing g_{AB} while the corresponding frequency $\Omega \approx 1.2$ is only weakly affected by the intercomponent coupling or the particle number. At negative moderate g_{AB} there is also a beating. The major amplitude mode, originally being an impurity mode (blue), evolves gradually into the majority component mode (red). The other mode appears just below $g_{AB} < -0.25$ and affects primarily the majority species.

The SMF fits well the lowest frequency at negative g_{AB} and at weak positive g_{AB} until the minimum is reached. Afterwards, it overestimates the frequency having larger deviations at stronger positive g_{AB}. We witness that SMF is incapable to identify an emerging mode at positive g_{AB}, though at negative g_{AB} it does register the beating behavior. It implies that the additional modes entering the dynamics at positive and negative g_{AB} are of a different character. Based on the insights gained in the previous section, namely, the presence of a breathing mode which is inaccessible to the SMF treatment, we conjecture that the additional mode emerging at positive g_{AB} stems from the hybrid sloshing mode $|N_A - 1, 1\rangle \otimes |0, 1\rangle$ at $g_{AB} = 0$ and $\Omega = 1.51$. Its contribution grows as the entanglement becomes stronger.

Next, let us focus on the case of a "narrow" impurity $\eta = 4$. The corresponding breathing spectrum is depicted in Fig. 9(b) for $N_A = 5$ and in Fig. 10(b) for $N_A = 10$ majority atoms. At $g_{AB} = 0$ we excite only the standard breathing mode of the impurity at frequency $\Omega = 8$ caused by the eigenstate $|N_A\rangle \otimes |0, 0, 1\rangle$. Considering the amount of available even parity eigenstates with energies up to eight quanta (40 for $N_A = 5$ and 45 for $N_A = 10$), one might naively think that many modes would be excited at finite g_{AB}. This is not the case as we count only up to six frequencies. They are well separated from each other and admit a convenient classification: impurity modes (blue) with $\Omega > 6$ and majority modes (red) with $\Omega < 4$.

The impurity features a beating composed of two modes at weak coupling. The gap between the corresponding frequencies grows with increasing g_{AB}. The one of smaller amplitude vanishes around $g_{AB} \approx 1.0$. The contribution of the other mode fades away quickly afterwards until it also disappears. At strong g_{AB} the impurity motion assimilates the majority component breathing. Both modes are reproducible by SMF ansatz, though SMF overestimates their contribution to the overall dynamics at strong g_{AB}.

Regarding the majority modes there is one with a nearly constant frequency ($\Omega \approx 2$) entering the dynamics already at weak coupling and making a large contribution to the majority motion across all coupling values. At weak g_{AB} it is accompanied by an oscillation of a smaller frequency. As the ground state is nondegenerate at $g_{AB} = 0$, this frequency corresponds to the gap between the two blue-colored frequencies. It also consistently disappears beyond $g_{AB} > 1$ along with the impurity modes. The latter are actually replaced by modes of lower frequency. One of them is of particular interest. It appears at $g_{AB} \approx 1$ for $N_A = 5$ and at $g_{AB} \approx 0.5$ for $N_A = 10$ gaining weight with increasing g_{AB}. The corresponding frequency is a linearly decreasing function of g_{AB}. It can be extrapolated to frequency $\Omega = 5$ at $g_{AB} = 0$, matching the energy gap between the ground state $|N_A\rangle \otimes |1\rangle$ and the hybrid sloshing mode eigenstate $|N_A - 1, 1\rangle \otimes |0, 1\rangle$. The entanglement is once again indispensable to account for the respective breathing mode.

To summarize, quenching a broad impurity excites less breathing modes barely affecting the majority motion. Quenching a narrow impurity excites more modes which are energetically well separated: high-frequency impurity-type and low-frequency majority-type modes. In both cases we evidence the presence of an entanglement-sensitive mode. It becomes relevant after some coupling threshold and can be traced back to a hybrid sloshing excitation $|N_A - 1, 1\rangle \otimes |0, 1\rangle$ at zero coupling.

D. Breathing of the first excited state

The Hamiltonian (1) has global reflection symmetry. The eigenstates are therefore separable into two classes of even and odd global parity. The quench operator does not violate that symmetry. Accordingly, an even global parity initial state can be expanded within the subspace of even eigenstates. The odd global parity space of the Hamiltonian has

its own "ground state," meaning the lowest-energy eigenstate of that subspace. If initialized in such a state, how will each species respond following our quench procedure? Will it be a few-mode breathing within each component, as for the even global parity ground state, or a more complex motion involving many modes? If only a few modes participate, how different are the respective frequencies as compared to the even global parity ground state?

To address the above questions, we start again with the example of a particle-balanced few-body Bose-Bose mixture (see Sec. IV A) at $\eta = 1$. There are several major differences regarding the odd global parity subspace. First, in the noninteracting regime the odd global parity "ground state" is twofold degenerate, composed of states where a single particle of either component is excited by one energy quantum: $|N_A - 1, 1\rangle \otimes |N_B\rangle$ and $|N_A\rangle \otimes |N_B - 1, 1\rangle$ with respect to harmonic oscillator basis. Once the degeneracy is lifted at finite coupling, the perturbed eigenstates can be distinguished by the c.m. quantum number. Since both states are likely to be populated after the quench, we need to consider each of them as a reference state when evaluating the energy gaps to the neighboring eigenstates. The frequencies of excited modes following a quench of the impurity trap will be contained within the set of these energy gaps. Second, the first-order breathing manifold for odd global parity subspace is composed of three quanta excitations at zero interaction. There are eight of them in total. Half of them are excitations within a single component: $|N_A - 1, 0, 0, 1\rangle$, $|N_A - 2, 1, 1\rangle$, and the same for B species. The other four distribute the three available quanta over both components: $|N_A - 1, 1\rangle \otimes |N_B - 2, 2\rangle$, $|N_A - 1, 0, 1\rangle \otimes |N_B - 1, 1\rangle$, and the other way around ($B \leftrightarrow A$).

In Fig. 11 we show the energy gaps between a reference state of even or odd c.m. parity (first or second column, respectively) and energetically closest eigenstates (c.m. quantum number indicated by color) as a function of the intercomponent coupling g_{AB} for three different intracomponent interaction regimes (rows).

Let us begin with the reference state of even c.m. parity (first column). First, there is a single constant frequency mode $\Omega = 2$ (blue dotted) for any interaction values. Second, there is a single frequency being a monotonically increasing function of g_{AB} (green dashed-dotted) and saturating to $\Omega = 3$ at strong positive g_{AB}. Third, among the three black solid curves there is one very weakly dependent on the interactions and it recovers to $\Omega = 2$ at strong positive g_{AB}, whereas the other two are highly susceptible to interactions and reach values beyond $\Omega = 3$. Finally, the lower red dashed curve represents the other reference state of odd c.m. parity. Regarding the frequencies of the remaining three red dashed modes, one of them behaves similar to the green dashed-dotted solid mode, while the other two are highly sensitive to interactions. Some of the crossings seen at $g_A = 0$ [Fig. 11(b)] among the black solid and red dashed curves become avoided at finite g_A [Figs. 11(a) and 11(c)] caused by broken-species exchange symmetry. Overall, most frequencies reach values above $\Omega = 2$ and there is nothing common to the breathing spectrum of the even c.m.-parity ground state (see Fig. 5) except the constant frequency mode.

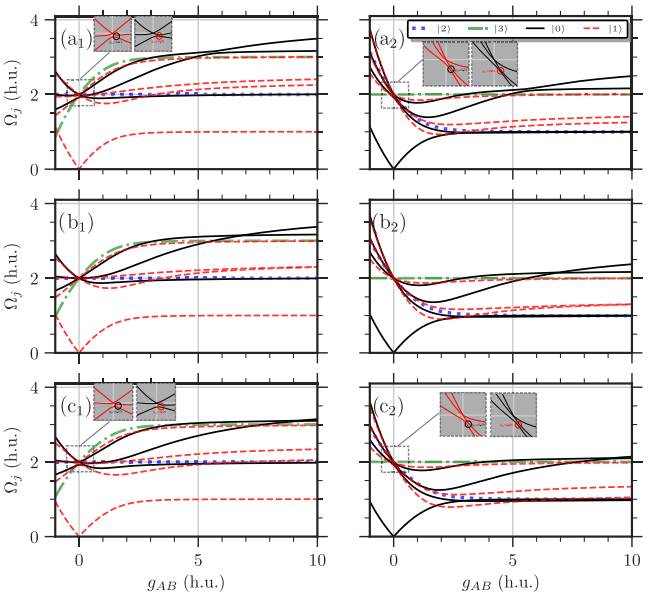

FIG. 11. Energy gaps $\Omega_j = |E_j - E_{\text{ref}}|$ with respect to lowest-energy reference eigenstates $|E_{\text{ref}}\rangle$ of odd global parity and even (first column) or odd (second column) c.m. parity in a few-body bosonic mixture $N_A = N_B = 2$. The gaps are functions of the intercomponent coupling g_{AB} at equal trapping frequency ratio $\eta = 1$, intracomponent interaction strength $g_B = 0$ for the second component, and (a) $g_A = -0.5$, (b) $g_A = 0$, (c) $g_A = 0.5$ for the first component. Whether the corresponding eigenstates are actually excited depends on the quench protocol. Different colors (line styles) refer to the center-of-mass (c.m.) quantum number in the eigenstate $|E_j\rangle$. The c.m. is a decoupled degree of freedom in this harmonic confinement. The insets represent a zoom-in on regions with avoided crossings which are indicated by circles and caused by $g_A \neq g_B$ asymmetry. Curves of different colors (line styles) may only cross. All quantities are given in harmonic units.

Focusing now on the reference state of odd c.m. parity (second column), we notice that all five frequencies encountered in Fig. 5 have here a corresponding match. The reason is that the reference state is a simple c.m. excitation, being a constant energy shift independent of the interaction strength. Correspondingly, the even global parity ground state and eigenstates responsible for the first-order breathing discussed in Sec. IV A are just spectrally shifted by a common constant. Thus, the corresponding energy gaps remain intact. The four black solid curves are the additional new modes. The lowest one corresponds to the even c.m.-parity reference state of odd global parity. There is one with a monotonically decreasing frequency and two of them are STP functions of g_{AB} very sensitive to interactions akin to the red dashed mode frequencies. In the Bose polaron setup there are two less "three-quanta" states since the two-particle excitations of the impurity are obviously excluded. However, there is also one more state, namely, a three-particle excitation $|N_B - 3, 3\rangle$ in the majority component. Thus, the first-order breathing manifold is composed of seven eigenstates in total. Now, we initialize an odd global parity ground state for the subsequent breathing dynamics (see representative examples in Fig. 12 to be compared with Fig. 6) and extract the frequencies of par-

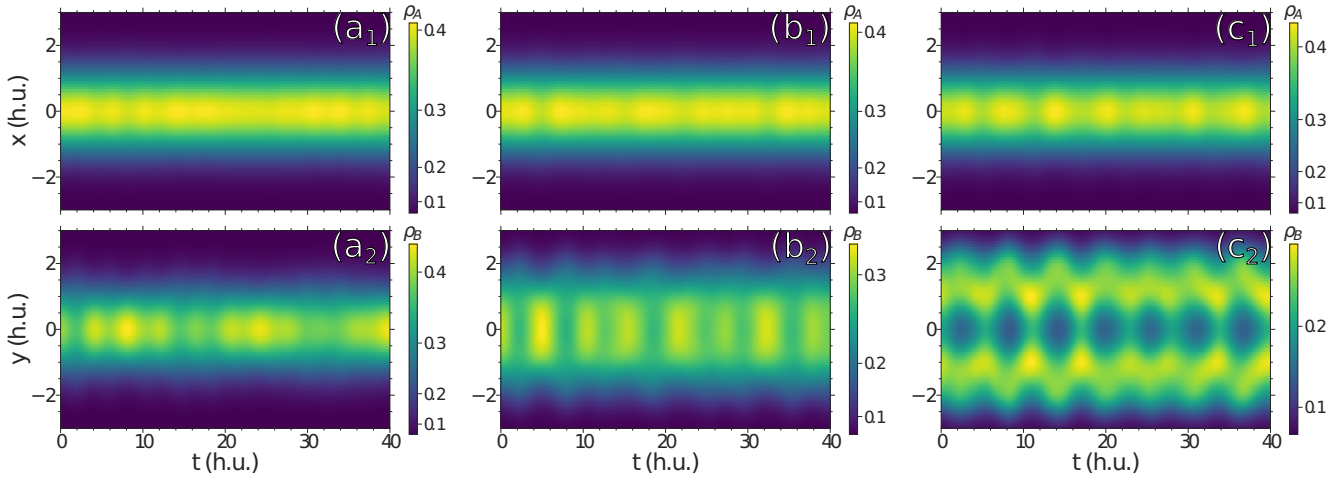

FIG. 12. Breathing oscillations of the one-body densities of the majority component $\rho_1^A(x)$ (first row) and the impurity $\rho_1^B(y)$ (second row) at a fixed majority-component interaction $g_A = 0.5$ for $N_A = 5$ and $N_B = 1$ particles initiated by preparation of the first excited state of odd global parity followed by an abrupt change of the trap ratio from $\eta = 1.05$ to 1. Columns 1–3 correspond to different intercomponent couplings: (a) $g_{AB} = 0.5$, (b) $g_{AB} = 1.0$, and (c) $g_{AB} = 1.5$. All quantities are given in harmonic units.

ticipating modes shown in Fig. 13. We immediately recognize the frequency pattern from Fig. 7. In particular, we evidence a coupling-insensitive Ω_A frequency at $\Omega \approx 2$, a monotonically decaying hybrid sloshing mode converging to $\Omega = 1$ and Ω_{AB} mode being an STP function of g_{AB}. There are, however, several differences. Importantly, both odd global parity reference eigenstates are participating in the dynamics, as indicated by the lowest-frequency curve. They are of opposite c.m. parity. Based on the excitation pattern (cf. Fig. 11) the odd c.m. reference state has a larger contribution than the one of even c.m.. Second, at weak positive g_{AB} the two odd global parity reference states are dominating the dynamics. The energy gap between them grows with increasing g_{AB} and approaches its limiting value $\Omega = 1$. Meanwhile, there is a gradual transfer of population to the hybrid sloshing eigenstate with a monotonically decaying frequency. Finally, at $g_A = 0.5$ and positive intermediate $g_{AB} \approx 1$ as well as at negative g_{AB} we identify some minor traces of additional modes absent for the even global parity ground state.

To summarize, the breathing response of an odd global parity ground state as compared to the actual ground state of even global parity displays notable differences in the density oscillations but bears strong similarity in the Fourier spectrum. We found an additional low-frequency mode of a mixed type arising from the degeneracy splitting of the odd global parity ground state.

V. SUMMARY

The breathing dynamics of a few-body Bose polaron in a one-dimensional species-selective parabolic confinement has been investigated in this work by means of the multilayer multiconfiguration time-dependent Hartree method for bosons. The dynamics has been triggered by a weak trap quench of the impurity for different intercomponent couplings g_{AB} ranging from weak attractive to intermediate repulsive values. The majority motion was affected indirectly via the majority-impurity interaction g_{AB}. We extracted the frequencies of excited modes from the breathing observables by using a compressed sensing algorithm. From this we constructed an averaged power spectrum and classified the modes according to their overall contribution to the dynamics. We also determined whether a mode is of majority or impurity type judged by the relative strength of respective observables in the averaged power spectrum. To highlight the importance of entanglement in our setup, we performed the same quench procedure for a species mean-field ansatz, which assumes that a wave function can be written as a single product state of combined majority coordinates and the impurity coordinate.

Different regimes of system parameters have been addressed. The majority component was noninteracting ($g_A = 0$), weakly attractive ($g_A = -0.5$), or weakly repulsive ($g_A = 0.5$) consisting either of $N_A = 5$ or 10 particles and different ratios of species trapping frequencies including equal localization length ($\eta = 1$), a "broad" impurity ($\eta = 0.51$), and a "narrow" impurity ($\eta = 4.0$) have been taken into account. Finally, we studied the impact of global parity symmetry on the breathing spectrum. To this end, we initialized the system in the first excited state having odd global parity as opposed to the ground state which is even.

For equal traps ($\eta = 1$) we detected up to *three* modes. First, at a weak majority-impurity interaction there is a two-mode beating. One mode is of a majority type. It does a comparatively small contribution to the overall breathing dynamics while its frequency is insensitive to g_{AB} variations, albeit depending on g_A and N_A. It reminds us of the Ω_A mode found in a few-body two-component mixture [88], though utterly flattened supposedly due to the particle-number imbalance and the absence of the complementary Ω_B mode. Interestingly, it becomes suppressed for a weakly attractive majority species at positive g_{AB}. The frequency of the second mode decreases monotonically as a function of g_{AB} until it bifurcates into two distinct frequencies. One of them keeps decreasing and becomes equally represented in both components. Other parameters such as majority-component interaction strength g_A or the number of majority atoms N_A

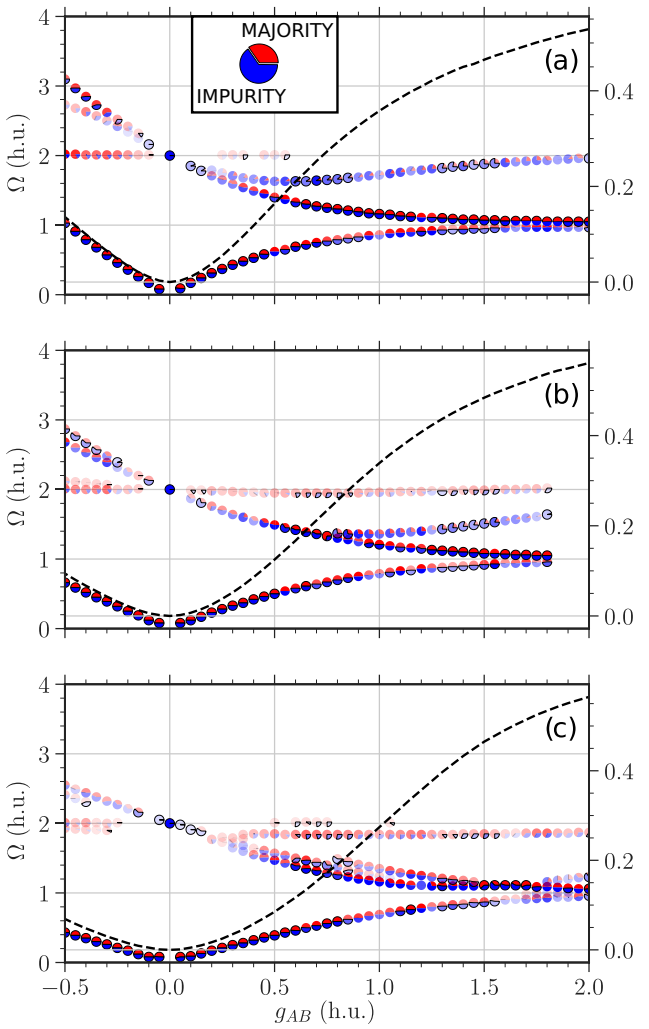

FIG. 13. Frequencies Ω of breathing modes excited by quenching the odd global parity ground state $|E_1\rangle$ of a Bose polaron $N_A = 5$ and $N_B = 1$ from a trap ratio $\eta = 1.05$ to 1.0 as a function of the intercomponent coupling g_{AB} for a fixed majority component interaction (a) $g_A = -0.5$, (b) $g_A = 0$, and (c) $g_A = 0.5$. Color coding as in Fig. 7. Black dashed line indicates the entanglement entropy S_{vN} of the initial state. All quantities are given in harmonic units.

barely affect this frequency. Why does the frequency behave this way? The corresponding mode is caused by an eigenstate of odd c.m. parity and even global parity. Its eigenenergy is independent of interactions. As the ground-state energy is a monotonically increasing function of g_{AB} and saturates at hard-core interaction, we obtain a monotonically decreasing energy gap between the two states. Importantly, it cannot be observed for species-symmetric trap quenches and is not a particular feature of the Bose polaron setup but of a two-component mixture in general. Furthermore, the entanglement needs to be taken into account to make the mode numerically visible as we demonstrate by a comparison to a species mean-field ansatz. The other frequency emerging out of the bifurcation bends and saturates back to the noninteracting frequency value with increasing g_{AB} while dominating the impurity motion. It reminds us of the coupling-sensitive Ω_{AB} mode found in a few-body two-component mixture [88], though here it appears to be much more sensitive to system parameters such as g_A and N_A.

By broadening the impurity trap ($\eta = 0.51$), only one mode can be excited at weak g_{AB}. It is of impurity type. The corresponding coupling-sensitive frequency features a minimum at positive g_{AB} and saturates at large g_{AB}. With increasing impurity-majority interaction, a beating emerges. At positive g_{AB} the additional mode is sensitive to the entanglement, while at negative g_{AB} both frequencies are well matched by the SMF ansatz. For a tightly trapped impurity ($\eta = 4$) up to six frequencies can be observed, though many more modes are in principle available. At weak g_{AB} we have two impurity-type modes and a single majority-type mode. The two impurity-type modes are of high frequency but are quickly fading away with increasing g_{AB}. At strong g_{AB} the impurity oscillations start imitating the majority motion. The lower-frequency majority-type mode has a large contribution to the ongoing dynamics except at very weak g_{AB}, while the corresponding frequency is rather insensitive to the intercomponent interaction. At finite positive g_{AB} we evidence the emergence of an entanglement-sensitive mode whose frequency is a monotonically decaying function of g_{AB}. Thus, the entanglement-sensitive mode is sustained even when the center-of-mass motion cannot be decoupled and, surprisingly, the corresponding frequency maintains its overall qualitative behavior.

Regarding the first excited state of odd global parity as an initial state for the breathing dynamics, we found the corresponding excitation spectrum to bear strong similarity to the one of even global parity ground state. It can be understood as follows. Some of the eigenstates lying in the odd global parity subspace have energies corresponding to the ones of even global parity subspace except for a constant energy shift, which is an integer number (in harmonic units) corresponding to a c.m. excitation. Nevertheless, there are also differences. For a weakly repulsive majority species and at intermediate g_{AB} we observe several additional modes absent in the ground-state spectrum. This is not surprising since the lowest-energy breathing manifold accessible to the first excited state is larger as compared to the ground state. Importantly, there is a slow-frequency mode equally represented in both components. It is caused by the degeneracy of the first excited state. For that reason, the frequency starts at $\Omega = 0$ when $g_{AB} = 0$. It saturates towards $\Omega = 1$ with increasing g_{AB} because the eigenenergy of the first involved state is a monotonically increasing and saturating function of g_{AB} while the second is independent of g_{AB}.

VI. CONCLUSIONS

Overall, the few-body Bose-polaron breathing spectrum has been studied and compared to the one of a particle-balanced Bose-Bose mixture. The species-asymmetric trap quench protocol employed in this work allowed to couple eigenstates of different c.m. parity (at $\eta = 1$) as opposed to a species-symmetric trap quench. We excited a different kind of a breathing mode. The eigenstate responsible for this mode can be traced back to a hybrid sloshing excitation $|N_A - 1, 1\rangle \otimes |N_B - 1, 1\rangle$ at zero interactions. We gave an

interpretation of the motion induced by this mode for a simple $1+1$ mixture: for a Gaussian background one-body density it induces a breathing motion while for a parity-symmetric two-hump profile we observe a simultaneous outward and inward sloshing motion of the two humps. The mode relies on the presence of entanglement, while its frequency is a monotonically decreasing function of g_{AB}. This opens the perspective to study the relation between the mode amplitude and the degree of entanglement, stored in the many-body composite state, adding yet another item into the analysis toolbox of breathing mode diagnostics.

ACKNOWLEDGMENT

M.P. gratefully acknowledges a scholarship of the Studienstiftung des deutschen Volkes.

[1] L. D. Landau, Phys. Z. **3**, 664 (1933).
[2] S. Pekar, Sov. Phys.–JETP **16**, 341 (1946).
[3] J. T. Devreese and A. S. Alexandrov, Rep. Prog. Phys. **72**, 066501 (2009).
[4] A. S. Alexandrov and J. T. Devreese, *Advances in Polaron Physics*, Vol. 159 (Springer, Berlin, 2010)
[5] G. D. Mahan, *Many-particle Physics* (Springer, New york, 2013).
[6] M. H. Anderson, J. R. Ensher, M. R. Matthews, C. E. Wieman, and E. A. Cornell, Science **269**, 198 (1995).
[7] K. B. Davis, M.-O. Mewes, M. R. Andrews, N. J. van Druten, D. S. Durfee, D. M. Kurn, and W. Ketterle, Phys. Rev. Lett. **75**, 3969 (1995).
[8] I. Bloch, J. Dalibard, and W. Zwerger, Rev. Mod. Phys. **80**, 885 (2008).
[9] C. J. Myatt, E. A. Burt, R. W. Ghrist, E. A. Cornell, and C. E. Wieman, Phys. Rev. Lett. **78**, 586 (1997).
[10] D. Blume, Rep. Prog. Phys. **75**, 046401 (2012).
[11] S. Palzer, C. Zipkes, C. Sias, and M. Köhl, Phys. Rev. Lett. **103**, 150601 (2009).
[12] J. Catani, G. Lamporesi, D. Naik, M. Gring, M. Inguscio, F. Minardi, A. Kantian, and T. Giamarchi, Phys. Rev. A **85**, 023623 (2012).
[13] T. Fukuhara, A. Kantian, M. Endres, M. Cheneau, P. Schauß, S. Hild, D. Bellem, U. Schollwöck, T. Giamarchi, C. Gross *et al.*, Nat. Phys. **9**, 235 (2013).
[14] N. Spethmann, F. Kindermann, S. John, C. Weber, D. Meschede, and A. Widera, Phys. Rev. Lett. **109**, 235301 (2012).
[15] N. B. Jørgensen, L. Wacker, K. T. Skalmstang, M. M. Parish, J. Levinsen, R. S. Christensen, G. M. Bruun, and J. J. Arlt, Phys. Rev. Lett. **117**, 055302 (2016).
[16] F. Meinert, M. Knap, E. Kirilov, K. Jag-Lauber, M. B. Zvonarev, E. Demler, and H.-C. Nägerl, Science **356**, 945 (2017).
[17] S. Nascimbène, N. Navon, K. J. Jiang, L. Tarruell, M. Teichmann, J. Mckeever, F. Chevy, and C. Salomon, Phys. Rev. Lett. **103**, 170402 (2009).
[18] A. Schirotzek, C.-H. Wu, A. Sommer, and M. W. Zwierlein, Phys. Rev. Lett. **102**, 230402 (2009).
[19] M. Koschorreck, D. Pertot, E. Vogt, B. Fröhlich, M. Feld, and M. Köhl, Nature (London) **485**, 619 (2012).
[20] C. Kohstall, M. Zaccanti, M. Jag, A. Trenkwalder, P. Massignan, G. M. Bruun, F. Schreck, and R. Grimm, Nature (London) **485**, 615 (2012).
[21] M. Cetina, M. Jag, R. S. Lous, J. T. M. Walraven, R. Grimm, R. S. Christensen, and G. M. Bruun, Phys. Rev. Lett. **115**, 135302 (2015).
[22] F. Grusdt and E. Demler, Quantum Matter Ultralow Temp. **191**, 325 (2015).
[23] F. Chevy and C. Mora, Rep. Prog. Phys. **73**, 112401 (2010).
[24] P. Massignan, M. Zaccanti, and G. M. Bruun, Rep. Prog. Phys. **77**, 034401 (2014).
[25] H. Fröhlich, Adv. Phys. **3**, 325 (1954).
[26] C. Chin, R. Grimm, P. Julienne, and E. Tiesinga, Rev. Mod. Phys. **82**, 1225 (2010).
[27] T. Köhler, K. Góral, and P. S. Julienne, Rev. Mod. Phys. **78**, 1311 (2006).
[28] A. G. Volosniev and H.-W. Hammer, Phys. Rev. A **96**, 031601(R) (2017).
[29] F. Grusdt, G. E. Astrakharchik, and E. Demler, New J. Phys. **19**, 103035 (2017).
[30] F. Grusdt, K. Seetharam, Y. Shchadilova, and E. Demler, Phys. Rev. A **97**, 033612 (2018).
[31] B. Kain and H. Y. Ling, Phys. Rev. A **98**, 033610 (2018).
[32] M. Drescher, M. Salmhofer, and T. Enss, Phys. Rev. A **99**, 023601 (2019).
[33] J. Jager, R. Barnett, M. Will, and M. Fleischhauer, Phys. Rev. Research **2**, 033142 (2020).
[34] M. Drescher, M. Salmhofer, and T. Enss, Phys. Rev. Research **2**, 032011(R) (2020).
[35] T. Giamarchi, *Quantum Physics in One Dimension*, Vol. 121 (Clarendon, Oxford, 2003).
[36] M. Olshanii, Phys. Rev. Lett. **81**, 938 (1998).
[37] T. Bergeman, M. G. Moore, and M. Olshanii, Phys. Rev. Lett. **91**, 163201 (2003).
[38] E. Haller, M. J. Mark, R. Hart, J. G. Danzl, L. Reichsöllner, V. Melezhik, P. Schmelcher, and H.-C. Nägerl, Phys. Rev. Lett. **104**, 153203 (2010).
[39] M. Girardeau, J. Math. Phys. **1**, 516 (1960).
[40] T. Kinoshita, T. Wenger, and D. S. Weiss, Science **305**, 1125 (2004).
[41] B. Paredes, A. Widera, V. Murg, O. Mandel, S. Fölling, I. Cirac, G. V. Shlyapnikov, T. W. Hänsch, and I. Bloch, Nature (London) **429**, 277 (2004).
[42] T. Sowiński and M. Á. García-March, Rep. Prog. Phys. **82**, 104401 (2019).
[43] O. E. Alon, R. Beinke, and L. S. Cederbaum, arXiv:2101.11615.
[44] U. Schollwöck, Rev. Mod. Phys. **77**, 259 (2005).
[45] L. Cao, V. Bolsinger, S. Mistakidis, G. Koutentakis, S. Krönke, J. Schurer, and P. Schmelcher, J. Chem. Phys. **147**, 044106 (2017).
[46] E. Bentine, T. Harte, K. Luksch, A. Barker, J. Mur-Petit, B. Yuen, and C. Foot, J. Phys. B: At., Mol. Opt. Phys. **50**, 094002 (2017).

[47] A. Barker, S. Sunami, D. Garrick, A. Beregi, K. Luksch, E. Bentine, and C. Foot, J. Phys. B: At., Mol. Opt. Phys. **53**, 155001 (2020).

[48] K. Keiler and P. Schmelcher, Phys. Rev. A **100**, 043616 (2019).

[49] M. Pyzh and P. Schmelcher, Phys. Rev. A **102**, 023305 (2020).

[50] M. Pyzh, K. Keiler, S. I. Mistakidis, and P. Schmelcher, Entropy **23**, 290 (2021).

[51] T. Lee, F. Low, and D. Pines, Phys. Rev. **90**, 297 (1953).

[52] F. Dalfovo, S. Giorgini, L. P. Pitaevskii, and S. Stringari, Rev. Mod. Phys. **71**, 463 (1999).

[53] J. Abraham and M. Bonitz, Contrib. Plasma Phys. **54**, 27 (2014).

[54] C. R. McDonald, G. Orlando, J. W. Abraham, D. Hochstuhl, M. Bonitz, and T. Brabec, Phys. Rev. Lett. **111**, 256801 (2013).

[55] H. Moritz, T. Stöferle, M. Köhl, and T. Esslinger, Phys. Rev. Lett. **91**, 250402 (2003).

[56] G. E. Astrakharchik, R. Combescot, X. Leyronas, and S. Stringari, Phys. Rev. Lett. **95**, 030404 (2005).

[57] T. Stöferle, H. Moritz, C. Schori, M. Köhl, and T. Esslinger, Phys. Rev. Lett. **92**, 130403 (2004).

[58] A. Altmeyer, S. Riedl, C. Kohstall, M. J. Wright, R. Geursen, M. Bartenstein, C. Chin, J. H. Denschlag, and R. Grimm, Phys. Rev. Lett. **98**, 040401 (2007).

[59] E. Haller, M. Gustavsson, M. J. Mark, J. G. Danzl, R. Hart, G. Pupillo, and H.-C. Nägerl, Science **325**, 1224 (2009).

[60] B. Fang, G. Carleo, A. Johnson, and I. Bouchoule, Phys. Rev. Lett. **113**, 035301 (2014).

[61] A. Di Carli, C. D. Colquhoun, G. Henderson, S. Flannigan, G.-L. Oppo, A. J. Daley, S. Kuhr, and E. Haller, Phys. Rev. Lett. **123**, 123602 (2019).

[62] D. Luo, Y. Jin, J. H. V. Nguyen, B. A. Malomed, O. V. Marchukov, V. A. Yurovsky, V. Dunjko, M. Olshanii, and R. G. Hulet, Phys. Rev. Lett. **125**, 183902 (2020).

[63] T. H. Johnson, M. Bruderer, Y. Cai, S. R. Clark, W. Bao, and D. Jaksch, Europhys. Lett. **98**, 26001 (2012).

[64] B. Huang, I. Fritsche, R. S. Lous, C. Baroni, J. T. M. Walraven, E. Kirilov, R. Grimm *et al.*, Phys. Rev. A **99**, 041602(R) (2019).

[65] P. T. Grochowski, T. Karpiuk, M. Brewczyk, and K. Rzążewski, Phys. Rev. Lett. **125**, 103401 (2020).

[66] S. Stringari, Phys. Rev. Lett. **77**, 2360 (1996).

[67] C. Menotti and S. Stringari, Phys. Rev. A **66**, 043610 (2002).

[68] A. Minguzzi and D. M. Gangardt, Phys. Rev. Lett. **94**, 240404 (2005).

[69] E. Quinn and M. Haque, Phys. Rev. A **90**, 053609 (2014).

[70] S. Bauch, K. Balzer, C. Henning, and M. Bonitz, Phys. Rev. B **80**, 054515 (2009).

[71] J. W. Abraham, K. Balzer, D. Hochstuhl, and M. Bonitz, Phys. Rev. B **86**, 125112 (2012).

[72] J. W. Abraham, M. Bonitz, C. McDonald, G. Orlando, and T. Brabec, New J. Phys. **16**, 013001 (2014).

[73] S. De Palo, E. Orignac, M. L. Chiofalo, and R. Citro, Phys. Rev. B **103**, 115109 (2021).

[74] S. Stringari, Phys. Lett. B **108**, 232 (1982).

[75] D. Ledesma, A. Romero-Ros, A. Polls, and B. Juliá-Díaz, Europhys. Lett. **127**, 56001 (2019).

[76] A. Rojo-Francàs, A. Polls, and B. Juliá-Díaz, Mathematics **8**, 1196 (2020).

[77] R. Schmitz, S. Krönke, L. Cao, and P. Schmelcher, Phys. Rev. A **88**, 043601 (2013).

[78] T. Keller and T. Fogarty, Phys. Rev. A **94**, 063620 (2016).

[79] A. I. Gudyma, G. E. Astrakharchik, and M. B. Zvonarev, Phys. Rev. A **92**, 021601(R) (2015).

[80] W. Tschischik and M. Haque, Phys. Rev. A **91**, 053607 (2015).

[81] M. Theisen and A. I. Streltsov, Phys. Rev. A **94**, 053622 (2016).

[82] Y. Y. Atas, I. Bouchoule, D. M. Gangardt, and K. V. Kheruntsyan, Phys. Rev. A **96**, 041605 (2017).

[83] B. D. Esry and C. H. Greene, Phys. Rev. A **57**, 1265 (1998).

[84] T. Busch, J. I. Cirac, V. M. Pérez-García, and P. Zoller, Phys. Rev. A **56**, 2978 (1997).

[85] A. Sartori and A. Recati, Eur. Phys. J. D **67**, 260 (2013).

[86] S. Peotta, D. Rossini, M. Polini, F. Minardi, and R. Fazio, Phys. Rev. Lett. **110**, 015302 (2013).

[87] S. Mistakidis, G. Katsimiga, P. Kevrekidis, and P. Schmelcher, New J. Phys. **20**, 043052 (2018).

[88] M. Pyzh, S. Krönke, C. Weitenberg, and P. Schmelcher, New J. Phys. **20**, 015006 (2018).

[89] S. Mistakidis, G. Koutentakis, G. Katsimiga, T. Busch, and P. Schmelcher, New J. Phys. **22**, 043007 (2020).

[90] S. Yip, Phys. Rev. A **64**, 023609 (2001).

[91] P. Siegl, S. I. Mistakidis, and P. Schmelcher, Phys. Rev. A **97**, 053626 (2018).

[92] K. Mukherjee, S. I. Mistakidis, S. Majumder, and P. Schmelcher, Phys. Rev. A **102**, 053317 (2020).

[93] K. M. Mittal, S. I. Mistakidis, P. G. Kevrekidis, and P. Schmelcher, Phys. Rev. A **102**, 013302 (2020).

[94] X. Andrade, J. N. Sanders, and A. Aspuru-Guzik, Proc. Natl. Acad. Sci. U.S.A. **109**, 13928 (2012).

[95] T.-L. Ho and V. B. Shenoy, Phys. Rev. Lett. **77**, 3276 (1996).

[96] H. Pu and N. P. Bigelow, Phys. Rev. Lett. **80**, 1130 (1998).

[97] S. Zöllner, H.-D. Meyer, and P. Schmelcher, Phys. Rev. A **78**, 013629 (2008).

[98] Y. Hao and S. Chen, Eur. Phys. J. D **51**, 261 (2009).

[99] F. Deuretzbacher, D. Becker, J. Bjerlin, S. M. Reimann, and L. Santos, Phys. Rev. A **90**, 013611 (2014).

[100] A. G. Volosniev, D. Petrosyan, M. Valiente, D. V. Fedorov, A. S. Jensen, and N. T. Zinner, Phys. Rev. A **91**, 023620 (2015).

[101] L. Cao, S. Krönke, O. Vendrell, and P. Schmelcher, J. Chem. Phys. **139**, 134103 (2013).

[102] S. Krönke, L. Cao, O. Vendrell, and P. Schmelcher, New J. Phys. **15**, 063018 (2013).

[103] J. Light, I. Hamilton, and J. Lill, J. Chem. Phys. **82**, 1400 (1985).

[104] M. H. Beck, A. Jäckle, G. A. Worth, and H.-D. Meyer, Phys. Rep. **324**, 1 (2000).

[105] A. Raab, Chem. Phys. Lett. **319**, 674 (2000).

[106] E. van den Berg and M. P. Friedlander, SIAM J. Sci. Comput. **31**, 890 (2009).

[107] I. Loris, Comput. Phys. Commun. **179**, 895 (2008).

[108] T. Busch, B.-G. Englert, K. Rzażewski, and M. Wilkens, Found. Phys. **28**, 549 (1998).